FACULTY OF ENGINEERING OF THE UNIVERSITY OF PORTO

UNIVERSITY OF BATH

Transducers to Detect Glioma Bursting Activity

Domingos Leite de Castro

Integrated Master in Bioengineering
Biomedical Engineering

Advisor: Paulo Ferreira da Rocha
Co-advisor: Paulo de Castro Aguiar

31/10/2018

Abstract

Recently, a new type of sensor displaying large area gold electrodes was successfully used to monitor populations of rat glioma C6 cell line, extracellularly. The large area leads to a very low background noise due to the decreased surface impedance, enabling the detection of the ultra-weak glioma signals. In this dissertation we developed and characterized large area electrodes coated with porous films. The rugosity enhances the sensing capabilities due to the increased effective area. Three devices were fabricated by evaporating circular gold electrodes on glass substrates and drop-casting dispersions of either poly(3,4-ethylenedioxythiophene):poly(styrenesulfonate) (PEDOT:PSS), carbon nanotubes (CNT) or a 1:1 mixture of both, over the electrodes. Atomic Force Microscopy measurements showed that CNT create the roughest electrode surface. On the other hand, the Electrochemical Impedance Spectroscopy results showed that PEDOT:PSS electrodes had the lowest interfacial impedance. A computer program was developed for the signal acquisition and analysis. The latter extracts the main parameters that characterize the spiking activity of the cell population – the inter-spike interval, spike amplitude and width – evidencing how these evolve with time. The technology developed was used to monitor and analyse the electric activity of a population of human glioblastoma-derived neural stem cells. The measurements were performed with the PEDOT:PSS/CNT sensor, combining the advantages of CNT and PEDOT:PSS. The background noise of the system had an amplitude of 0.4 pA peak-to-peak, significantly better than that obtained with gold electrodes. With the developed software, the self-induced cooperative electric activity of human glioma populations was characterized for the first time.

Acknowledgments

I would first like to thank to my thesis supervisor Dr. Paulo Rocha for his guidance and support during my stay at the University of Bath, UK. Paulo was always there to provide prompt and efficient solutions to all the difficulties and constrains that I faced during my work. His trust and enthusiasm motivated me to push beyond my limits, making me a better student – and researcher – than I ever though I could be. I would also like to acknowledge my co-supervisor Dr. Paulo Aguiar for his concern and availability to assist in whatever was needed.

I would like to thank to my co-worker and friend Uros Zupančič for helping me in the lab with the development of the devices, to Aya Elghajiji, for her valuable work preparing the cell cultures, to Miguel Valverde for helping me with the recordings and to the Senior Technician Dr. Siva Sivaraya for instructing me in the evaporation of the gold electrodes and for all the technical support in the lab. A special thank to all the members of the Biosensors group of the University of Bath for their friendship and support: to Chon Samrit, my dear friend, tennis partner and travelling companion, to Dr. Shu Jiang, Dr. Gorachand Dutta, Şerife Üstüner, Jahnavi Jha, Sotiris Papamatthaiou, Joshua Rainbow, Stefan Chindea and the group leaders Dr. Pedro Estrela and Dr. Choupina Moschou.

To my dear flatmates and friends, Ben, Fionn, Sam and Tom who made my stay in England so enjoyable and fun – until next time.

Finally, to my loving parents and my three beautiful sisters, who have always supported me in my studies and in all my personal projects and ambitions. Thank you for giving me the strength to fight for what I want.

Domingos

Contents

List of Figures

Abbreviations

AFM	Atomic Force Microscopy
ASIC	Acid-Sensing Ion Channels
CNS	Central Nervous System
CNT	Carbon Nanotubes
DMSO	Dimethyl Sulfoxide
EIS	Electrochemical Impedance Spectroscopy
FP	Field Potential
GNS	Glioblastoma-derived Neural Stem cells
GOPS	(3-glycidyloxypropyl) trimethoxysilane
ISI	Inter-Spike Interval
LBE	Large Bi-Electrodes
MEA	Micro-Electrode Array
PEDOT	Poly (3,4-ethylenedioxythiophene)
PSS	Poly (styrene sulfonate)
SNR	Signal-to-Noise Ratio

1 Introduction

The new field of Neuroengineering is focused on studying the neural circuitry of the Central Nervous System (CNS) by employing engineering technologies. One of its primary objectives is to understand the relation between the dynamics of the brain signalling and its associated physiological functions/pathologies. Neurons have always been the main target of neurological research. However, they are not the only cells of the brain involved in the mechanisms of information processing. In the mid-1800s a new type of brain cells was discovered – glial cells.

For decades glia was seen as mere "glue" that provided structural support to neurons, however, recent research shows that they engage in specialized communication between other glial cells and neurons [1]. Nonetheless, much is still unknown about the neuron-glia interaction. This knowledge gap is, in part, due to the ultraweak electrical activity displayed by glial cells and the lack of tools available to measure it. Micro-Electrode Array (MEA) systems are the standard methodology used for long time recordings of neuron populations. They comprise dozens of micro-sized electrodes (usually 60 or 64 electrodes with 10 to 30 μm of diameter), ensuring a good spatial resolution. However, the small area of the electrodes leads to a significant background noise. This imposes severe measuring limitations. MEAs can only detect signals with high amplitude and frequency, such as the action potentials of neurons. Glial cells, however, display very weak and low frequency electric activity which cannot be detected with this method.

Low frequency signalling has been correlated with brain disorders like epilepsy and schizophrenia [2], [3]. There is a strong need for devices that monitor the weak and slow activity of brain cells. With such devices one could study the electrical behaviour of glia populations and understand whether certain brain disorders are caused by their abnormal signalling. The frequent correlation between gliomas and epileptic seizures may well be one of these scenarios. Glioma is a severe brain tumour of glia cells and accounts for approximately 80% of all malignant brain tumours [4]. Gliomas frequently lead to epileptic seizures. Epilepsy is estimated to affect approximately 0.8% of the population, where 30% of the cases derive from underlying neurological disfunctions (symptomatic epilepsies) [5]. It is characterized by the occurrence of unpredictable seizures which occur due to a hypersynchronous high-amplitude low-frequency bursting activity of neuronal cells [6], [7]. The risk of seizures in glioma patients varies between 40% and 100%, depending on the type of glioma [8]. Glioma-related epilepsy has an unfavourable clinical course when compared to other types of symptomatic epilepsies.

The specific pathophysiological mechanisms of the seizures are multifactorial and not fully understood yet [9]. Medical anti-epileptic treatment for patients with glioma-related epilepsy is met with limited success and about one-third of patients with epilepsy still have poor seizure control [10],[11]. This is mainly due to lack of knowledge on the underlying epileptogenic pathways. Many

epileptogenic mediators related with gliomas have already been identified, such as: the direct mechanical effects of the space-occupying tumour [12]; changes in synaptic vesicles and glial gap junctions [13]; loss of inhibitory synapses on pyramidal neurons [14]; imbalance between excitatory and inhibitory factors, particularly with the excitatory neurotransmitter glutamate released by glioma cells [15]–[17]. However, little is known about the electrical behaviour of glioma cells and the way it may influence the neuronal firing. A better understanding of the electrical signalling of glioma populations may provide new insights about the epileptogenic mechanisms associated with the tumour. This justifies the development of new devices capable of monitoring such activity for long periods of time, since the traditional methods fail to accomplish so.

Very recently, a breakthrough methodology made this possible for the first time. It was accomplished by using electrodes with very large surface area, in the order of mm^2. The large area leads to very low impedance at the electrode surface, increasing the sensitivity by several orders of magnitude. Instead of having an array of electrodes like MEAs do, there is only a measuring electrode and a counter electrode, establishing a Large Bi-Electrode (LBE) system. The measuring electrode encompasses an entire population of adherent cells and, therefore, the signal recorded corresponds the global activity of the cell population. Associating this novel sensor with a very sensible and low-noise signal conditioning setup gives rise to a system capable of viably detecting ultra-weak cell signals.

The LBE paradigm was already tested with different types of cell populations that display low frequency activity such as gliomas [18]–[20], astrocytes [21] and even a zebrafish hearts [18]. It is a recent and promising approach with a wide margin for improvement. LBE systems can be upgraded both in terms of the sensor itself and the associated software for signal acquisition and analysis.

Regarding the sensor, improvements should be focused in enhancing the sensitivity, biocompatibility and chemical stability of the electrodes. This can be achieved with the use of conducting polymer coatings on the electrodes such as poly(3,4 ethylenedioxythiophene):poly(styrenesulfonate) – PEDOT:PSS. PEDOT:PSS-coated electrodes outperform state-of-the-art metal electrodes. This polymer lowers the impedance of the sensing surface and improves the cell coupling, facilitating the signal transduction from cells to the electrodes [22], [23]. MEAs with PEDOT:PSS coatings are commercially available, and PEDOT:PSS-coated LBEs have already been tested [24]. However, PEDOT:PSS films exhibit weak mechanical stability and poor adhesion to the underlying substrate. Carbon Nanotube (CNT) coatings too offer an exciting alternative due to their mechanical stability, chemical durability, electrical conductance and biocompatibility [25]–[28]. Gold micro-electrodes coated with PEDOT:PSS/CNT composites were reported to have increased porosity and mechanical stability when compared to PEDOT:PSS coatings only [29]. For this reason, a PEDOT:PSS/CNT film is expected to improve the surface properties of LBEs as well. This type of LBE was not yet implemented, to the best of our knowledge.

As for the software, an efficient tool to acquire and analyse the signals is paramount for the end user of the developed devices. Commercially available MEAs, for instance, have specific programs that enable an intuitive acquisition and analysis of signals. The signal analysis software is particularly important when dealing with long time recordings, which may contain hours or even days of acquired data. When equipped with the proper algorithms, they may provide a general view of the dynamics of the cell population activity. Since the signals of glioma populations are only recently being captured and analysed, it is essential to have adequate software to characterize them. Ideally, this tool should provide an overview of how the periodicity, amplitude and width of the spikes vary over time – these are the main parameters that characterize the bursting activity of the cells.

The presented project aims to improve the LBE methodology in the two fronts stated above – sensor improvement and software development. The main objectives of this thesis are:

- Develop improved LBEs by using PEDOT:PSS and/or CNT coatings over the electrodes;
- Characterize the developed sensors in terms of their electrophysiological properties and surface topography;
- Develop an acquisition software to monitor and save the detected signals;
- Develop a signal analysis program to characterize the evolution of the cells' activity;
- Use the developed hardware and software to measure and analyse cooperative electric activity of human glioma stem cells for the first time.

The dissertation is structured as follows: Chapter 2 explains the relevant theoretical fundamentals of neurobiology, electrophysiology and biomaterials that must be clarified to later understand what was achieved with this project and why; Chapter 3 is focused on the sensor fabrication and characterization; Chapter 4 presents the software developed for signal acquisition and analysis; Chapter 5 is dedicated to the cell measurements, describing the experimental setup used in the recordings, the cell culture used and the measurements results obtained; Chapter 6 concludes this dissertation and presents the future work.

2 Theoretical Background

This opening section aims to provide the reader with the background knowledge required to fully understand the necessity, objective and constraints of this project. As mentioned in the introduction, the main goal is to develop and characterize a new type of biosensor – LBEs coated with PEDOT:PSS and/or CNT films – and use it to monitor the electric activity of glioma populations. There are several concepts in the realm of neurobiology, electrophysiology and biomaterials that must be properly introduced before moving on with the description of the work developed. The theoretical explanations will be followed by the associated literature review, framing this thesis in the state-of-the-art of the research field.

This chapter will be divided in the following sections: 1) brief explanation of the relevant aspects of the neurobiology, with focus on the electric activity of glial/glioma cells and how they differ from the commonly studied neuronal signals; 2) description of the electrophysiological devices used to monitor cell activity, focusing on the main constraints involved and why they restraint the detection of the glial/glioma activity; 3) introduction of the LBE concept, explaining why the ultra large electrodes enable the recording of these signals, and exposing some of the first monitoring results obtained with this new paradigm; 4) overview of the PEDOT:PSS and CNT as electrode coatings to improve the surficial properties.

2.1 Electric Activity of Neurons and Glial Cells

Glial cells – also referred to as neuroglia or glia – are non-neuronal cells that constitute a large fraction of the mammalian brain, being as numerous as neurons [30]. They are mainly divided into oligodendrocytes, astrocytes and microglia. For many decades after being discovered, they were thought to only provide structural support to neurons. However, since the early 1980s there has been a continuous shift from this misconception [31]. They are now known to have an active role in maintaining the brain homeostasis. Their functions include, amongst others, structural support of neural cells, formation of myelin sheaths in the CNS, secretion and absorption of neural transmitters and maintenance of the blood–brain barrier [32], [33]. Figure 2.1 illustrates how the different types glial cells are physically related with neurons: astrocytes are usually in contact with the axonal track; microglia, the smallest of the glial cells, are in contact with the upper region of the neurons (body cell and dendrites); oligodendrocytes extend their processes around the axon wrapping it with myelin sheath.

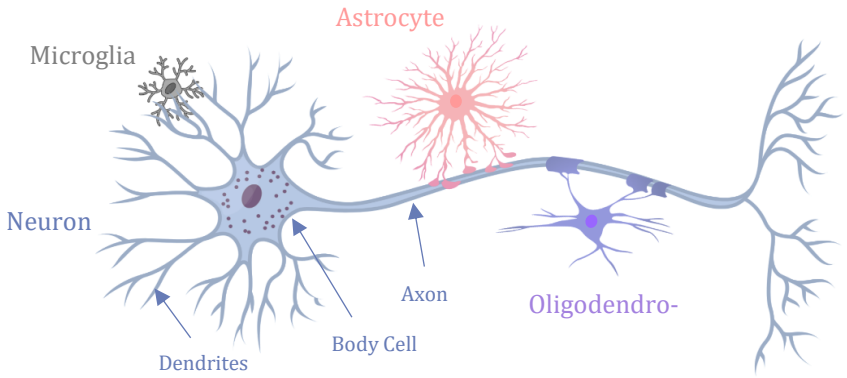

Figure 2.1 Representation of an Astrocyte (pink), an Oligodendrocyte (purple), a Microglia cell (grey) and a Neuron divided in dendrites, body cell and axon (blue).

Recent studies have shown that glia cells are not electrically silent, as was erroneously conceived for many decades [34]. They engage in bidirectional crosstalk with neurons. Understanding the dynamics of glial electric activity would provide meaningful insights about the neuron-glia communication and their mutual regulation. However, monitoring the activity of glial/glioma populations is a particularly challenging task in the realm of neurological electrophysiology. To understand why, we must first comprehend how these signals differ from the traditionally acquired neuronal electrical bursts. The amplitude and frequency of glial electrical spikes are significantly smaller than that of neuronal action potentials. We will start by describing the chemical and electrical processes that lead to the neuronal spikes, and the different membrane structures involved. The signalling mechanisms of glia, and specially glioma, are far from being fully understood. However, some of the membrane structures involved in neuronal bursts can also be found in glial membrane, therefore, the firing processes must be analogous.

Just like in all animal cells, the intracellular potential of neurons at rest is approximately 70mV lower than the extracellular potential due to the unbalance between the concentration of Na^+ and K^+ inside and outside the cell. Neurons are composed by three main parts: dendrites, cell body and axon (see Figure 2.1). The dendrites receive chemical signals from adjacent neurons via neurotransmitters in a process called synapse. The receptors of neurotransmitters induce the intake of positive ions in the cell body. Special types of transmembrane proteins called voltage-gated ion channels are sensible

to changes in membrane potential and will open to allow the free passage of specific ions according to their concentration gradients. The sequential opening and closing of the Na^+ and K^+ voltage-gated ion channels make the membrane potential rise to 40 mV and then drop to the resting state again. This impulse is called action potential and unfolds in approximately 3 ms. Adjacent voltage-gated ions are activated by the action potential, repeating this process along the axon. When the electric signal reaches the extremity of the cell it induces the opening of Ca^{2+} ion channels. The entrance of Ca^{2+} into the cell leads to the release of neurotransmitters, generating a chemical signal that will stimulate the following neuron.

Neurons have other types of ion channels besides the voltage-gated ones. Acid-sensing ion channels (ASICs), for instance, become permeable to specific ions at low pH. Ligand-gated ion channel do so when bonded to specific chemical messengers.

The electric activity of neurons is very well defined and pronounced. The same does not apply to glia. Glial cells have many of the same voltage-gated Na^+, Ca^{2+}, K^+ and Cl^- channels [35]–[38], and neurotransmitter receptors found in neurons [39]. However, the density of these channels is about 1000 times lower than in neurons, thus making glial cells uncapable of substantially depolarizing their membranes [40]. For this reason, they have been called non-excitable cells. The ionic fluctuations generated in the membrane of astrocytes are approximately 1000 times weaker and slower than the neuronal action potentials, having an amplitude of few microvolts and lasting for several seconds [21]. Recent studies identified the presence of ASICs in different types of glial cells, making their membrane permeable to Na^+ or Ca^+ at low pH [41]–[43]. They can also shape the neuronal signal transmission by several means such as buffering the K^+ release in neurons [44] or absorbing neurotransmitters like glutamate. Calcium waves are particularly relevant in this glia-neuron communication. An intracellular increase of Ca^{2+} in astrocytes induces them to release neurotransmitters [45]. More, these cells display an exchangeability between Ca^{2+} and Na^+ signals – the first consists in a chemical signal and the second manifests itself as electrical currents. This is due to membrane proteins capable of interchanging or amplifying the flow of these ions [46].

Glioma cells too have voltage-gated ions channels and ASICs [47]–[49]. Like glia, glioma cells are not able to generate action potentials and display only weak electric activity. However, it has been stated that the electrical properties of certain types of glioma cells (glioblastomas and oligodendrogliomas) are closer to that of neurons than to normal glial cells – upon an intracellular current injection these cells respond with a significant electrical activity due to the high density of voltage-gated ion channels on these cells [50]. Nonetheless, the fact that individual glioma cells can produce strong electric signals when properly stimulated does not mean that such events occur autonomously in a real multicellular brain glioma. Actually, such behaviour was never reported until the date.

So, the cells exhibit electric signals in different ranges of magnitude and frequency. Glial and glioma cells are characterized by weak membrane fluctuations, orders of magnitude smaller than the neuronal action potentials. These findings were made possible by directly measuring the potential difference across the membrane of individual cells, with highly sensible electrophysiological technique. However, the interconnective behaviour of cell populations cannot be inferred from the results obtained with individual cells. Recently, the goal has been to develop devices that monitor the activity of entire populations *in vivo* or *in vitro* for long periods of time. This imposes a great technological challenge, especially when measuring the weak electric activity of glia/glioma populations, as explained in the next section.

2.2 Electrophysiological Devices for Cell Monitoring

The electrical stimulation and recording of neuronal cells can be performed intracellularly or extracellularly. Intracellular recordings are used to measure the electrical current or potential drop across a cellular membrane, with or without stimulation. There are several variations but they all involve connecting one electrode directly to the cell membrane while having a reference electrode outside the cell. It is a very sensible and precise method due to the high cell coupling established. A higher cell coupling increases the ratio between the amplitude of the recorded signal and the amplitude of the signal originated by the cell – the measurement is less attenuated [51]. In intracellular recordings this ratio is approximately 1 – almost perfect coupling. This enables the detection of the entire range of signals generated by cells: from the ultra-weak and slow membrane fluctuations of glial cells, to the bursting action potentials of neurons. Intracellular recordings have two main limitations: they can only monitor individual cells, and for short periods of times (few hours). These limitations make this methodology useless for the purpose announced: monitoring populations of glia/glioma cells for long periods of time.

The circuit-connectivity, activation sequences, physiology and pathology of neuronal systems are mainly studied with the use of MEAs, *in vivo* and *in vitro* [51]. These devices contain multiple micro electrodes, through where the signals of adhered cells are captured extracellularly. With these method it is possible to record and stimulate populations of cells over days or even months [52]–[55]. They are typically made of gold, platinum or indium tin oxide, composed by 60 or 64 planar electrodes with diameters between 10 and 30 μm. Unlike the intracellular recordings, planar MEAs do not inflict any damage to the cellular membrane. On the top of that, the recordings performed with these devices contain spatial information. By exhibiting multiple electrodes, it is possible to acquire the signals from several clusters of cells, or individual cells, depending on the size of the electrodes. This way, one can trace the firing dynamics and connectivity of the neuronal system. Ideally, a MEA should be able to track the entire range of electric activity of individual neurons – it should have high sensitivity, low background noise and high spatial resolution. This ideal balance is dependent on three main factors: cell coupling, electrode area and electrode/electrolyte impedance.

The cell coupling in planar MEAs is considerably poor because the cells are not in direct contact with the electrodes' surface. There is always a cleft formed between both, with a typical thickness of 40–100 nm [56]–[58] filled with the electrolyte. So, instead of recording the potential across the membrane (as the intracellular recordings do), MEAs measure what is called field potentials (FP). FP are signals that result from the sum of all the electrical current generated by nearby neurons or glial cells. In conventional MEAs, the signal acquired is significantly attenuated, having a magnitude of about 0.1–1% of the associated membrane potential. This significantly limits the range of measurable signals: only the action potentials can be clearly detected. MEAs are "blind" to weaker signals. The sensitivity of the recording is inherently limited by the fact that the measurement is made extracellularly.

On the top of that, the FPs reflect the superposition of all the electric activity occurring over an electrode. Depending on its area, the FP can be the result of the activity of either one, or several neurons and glial cells. It is not trivial to isolate the different components of the signal if it was shaped by multiple cells. This issue can be "solved" by lowering the size of the electrodes, to guarantee that only one cell adheres to its surface. The increased spatial resolution is very useful to study the firing dynamics of the neuronal systems. However, decreasing the area will increase the impedance of the

electrode/electrolyte interface leading to a higher background noise. This is due to the increase of thermal noise, as explained below.

Thermal noise is associated with the random movement of electrons in a conductor due to the effect of temperature. Its mean amplitude can be expressed as

$$V = \sqrt{4kTR\Delta f} \tag{1}$$

where k is the Boltzmann's constant, T is the temperature in Kelvin, R is the real part of the impedance (the resistance), and Δf is the frequency bandwidth. Equation 1 shows that the thermal noise increases with the resistance. The resistance of a given material with a cross sectional area A, length l and electrical resistivity ρ can be described by Pouillet's Law as shown in Equation 2:

$$R = \rho \frac{l}{A} \tag{2}$$

In an electrode, the cross-sectional area shown in Equation 2 corresponds to the surface area. So, decreasing the diameter of the electrode will increase the resistance at its interface with the electrolyte. Therefore, from Equation 1, it can be deduced that there is an inverse relation between the surface area and the thermal noise.

State-of-the-art MEA systems exhibit a background thermal noise that may vary between 10-40 μV (depending on the material and area of the electrodes) [59],[60]. This defines their detection limit. The collected signal is commonly filtered with a band pass of 20–2000 Hz [61]. Only the high frequency cellular events are detected, such as the FPs associated with action potentials (the only signals strong enough to be properly detected anyway).

The signal-to-noise ratio (SNR) ratio can be optimized by modifying the electrode's surface. The goal is to increase its effective sensing area (leading to less interfacial impedance and, therefore, thermal noise) and improve the cell coupling (lowering the signal attenuation). To achieve this, research has been focused on the use of porous materials such as platinum black, carbon nanotubes (CNT) and conductive polymers [62]. The rough topography of the surface increases the effective area which decreases the background noise. Also, the cell adhesion is optimized because, when compared to planar metal-based electrodes, the chemical, mechanical and topographical properties of these soft and rough surfaces are closer to the properties of the extracellular matrix [63]. As a result, the attenuation of the recording decreases since the thickness of the cleft between the cell and the electrode is minimized. More sophisticated and complex techniques focus on creating three-dimensional microstructures on the surface of the electrode, such as micro-sized gold mushrooms-shaped arrays [64], [65] or nanopillar arrays [60], [66]. These structures provide physical support for the cells to attach and involve, assuring a considerably high cell coupling.

To conclude, spatial resolution and SNR are inversely related and need to be properly balanced according to the final purpose of the device. The prime goal of MEAs is to detect the action potentials generated by single neurons in large neuronal circuits. The associated cost is that the FPs generated by the slow and weak activity of glia/glioma cells cannot be properly detected with this technique. The amplitude and frequency of their signals are below the measurable ranges of MEAs because: 1) all the signals measured are significantly attenuated due to the poor cell coupling; 2) the magnitude of the noise generated by the microscale electrodes is higher than the FPs generated by the membrane fluctuations; 3) the filters applied to minimize the noise cut-off the residual glial activity. A new extracellular methodology is required to measure populations of glial cells extracellularly for long periods of time.

2.3 The New Paradigm: Large Bi-Electrodes

MEAs, the standard electrophysiological methodology for long-term recordings of neuronal populations, are unable to detect the activity of glial/glioma populations. The spatial resolution/SNR duality needs to the reconsidered if the objective is to detect ultra-weak signals. The background noise of the recording must be very low, ideally below 1 μV [21]. The noise is originated by the instrumental noise and that electrochemical noise of the electrode/electrolyte interface [19]. The latter can be seen as an effect of the thermal noise, as already explained, and decreases with an increasing area. So, the simplest way to effectively measure these ultra-weak signals is to sacrifice the spatial resolution in behalf of the SNR by using a pair of very large area electrodes, mentioned here as Large Bi-Electrodes (LBE).

The signal captured with LBEs is the superposition of the electrical activity generated by each cell adhered to the electrode. It is then possible to detect the cooperative activity of the population: synchronized cell signalling appears as defined peaks, while the random, uncorrelated activity of the population is translated into an increased background noise. The superimposed activity of the adhered cells generates a much more powerful (and detectable) signal. Unlike MEAs, LBEs are not meant to study the interconnectivity and firing of individual cells. Instead the purpose is evaluating whether a given population manifests cooperative electric behaviour, and under which conditions. In this section it will be discussed: 1) the equivalent circuit model of the system cells-LBE, and the effect of the large area in the parameters of the modelled circuit; 2) the relevant results already achieved in literature by employing this method to measure glioma activity.

2.3.1 Equivalent Circuit Model: Measuring in Current Mode

Equivalent circuit models are extremely useful to understand how the elements of a given system are electrically related. The system cells-electrolyte-transducer can be electrically modelled according to the circuit shown in Figure 2.2.

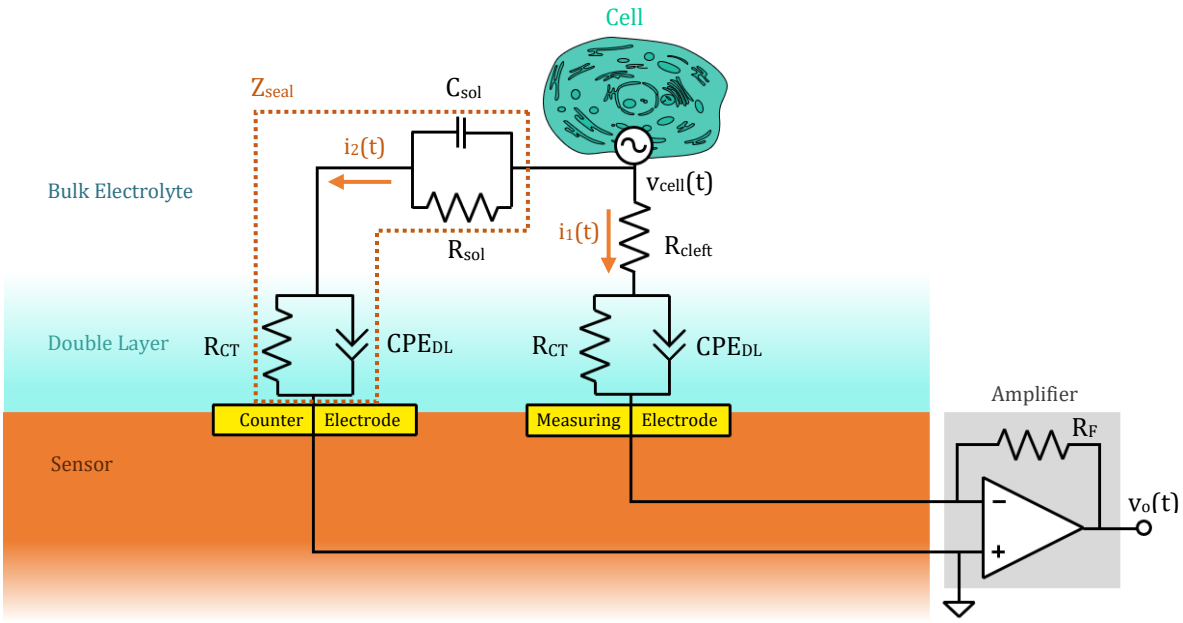

Figure 2.2. Equivalent circuit model formed by the cell, electrolyte, LBE and amplifier (the different elements of the figure are not to scale).

It is important to understand how the different components of the illustrated circuit influence the propagation of the signal since it is generated at the cell membrane until it reaches the amplification stage. This way, we can analyse which can be optimized and how, in order the obtain a better SRN. The analysis will be focused on the effect that the large electrode area has on the performance of the measuring system.

The cell membrane is seen as an AC voltage source generating a signal $v_{cell}(t)$ that is spread through the electrolyte. As shown in Figure 2.2, there is no direct contact between the adhered cells and the electrodes. A cleft filled with medium is formed between the cell and the electrode with a thickness of 40-100 nm. The associated resistance, R_{Cleft}, leads to a considerable attenuation of the signal. It is a function of the width of the gap, the sensing area of the electrode and the conductivity of the electrolyte. Large area electrodes minimize the resistive effect of this cleft. As a result, the electrical coupling between the cell and the electrode, one of the most critical parameters of electrophysiological sensors, is significantly improved.

At the electrode-electrolyte interface there are two physical phenomena responsible for the current transference, referred to as faradaic and non-faradaic reactions. Faradaic reactions are associated with the oxidation/reduction of the metal surface (usually gold) when in contact with an electrolyte. These reactions lead to the exchange of electrons between the two phases, therefore propagating the current. This charge transference has an associated resistance R_{CT} which is expressed by:

$$R_{CT} = \frac{RT}{nFJ_0} \tag{3}$$

where R is the gas constant, T is the absolute temperature, n is the number of electrons involved in the redox reaction, F is the Faraday constant and J_0 is the current density. Considered a noble metal in the realm of electrochemistry, gold electrodes have very weak faradaic reactions. Hence, the associated charge transference resistance is very high, significantly higher than the cleft resistance R_{cleft}, for instance. The value of R_{CT} is normalized to the electrode area (the element J_0, which represents the current per unit of area) so it not expected to change significantly with the enlargement of the electrodes.

Unlike the faradaic reactions, in the non-faradaic reactions there is no exchange of electrons between the electrode and the electrolyte. An electrical double-layer is formed at this interface due to the accumulation of charges in the electrode's surface. The charge accumulation can be a result of: 1) the excess/lack of electrons at the metal surface which attracts the ions/anions from the electrolyte; 2) the specific chemical adherence of some ions to the electrode´s surface; 3) the polarity of certain molecules, which lead to a preferential orientation when adhering to the metal. This double layer formed at the interface has a capacitive effect: analogously to the plates of a capacitor, the current is propagated between the electrode and the electrolyte without the actual crossing of charges between the two phases. However, empirical evidence shows that this capacitive effect is not modelled by a perfect capacitor. The polarization capacitance of the double layer is frequency dependent and is better described as a constant phase angle element (CPE), denominated here as CPE_{DL}. The impedance associated with a CPE is given by the empirical relation shown in Equation 4 [67]:

$$Z_{CPE}(\omega) = \frac{1}{(j\omega Q)^n} \tag{4}$$

where Q represents the magnitude of the capacitive effect as a frequency independent phenomenological parameter with the units $Fcm^{-2}s^{n-1}$ (the units of Q have no real physical meaning), n is a constant associated the homogeneity of the surface ($-1 \leq n \leq 1$), and $w = 2\pi f$. For an ideal surface, n = 1, the double layer behaves as an ideal capacitor. For n = 0, CPE represents a resistor and for n = – 1, it corresponds to an inductor. The value of n is typically 0.8 for biomedical electrode systems [68]. The physicochemical cause for this deviation from the ideal state is not fully understood yet. It is known to be associated with the roughness of the surface since liquid metal electrodes with perfectly homogenous surface behave as an ideal capacitor with n = 1 [69]–[72]. The capacitive effect of the double layer increases with the area of the electrode – the value of Q is directly proportional to the effective electrode area.

Considering both types of reactions occurring at the electrode-electrolyte interface, one can conclude that an increased electrode area leads to a lower interfacial impedance, mainly due to the higher capacitance. This lowers the interfacial impedance and, consequently, the thermal noise as already discussed in section 2.2, increasing the SNR.

The two electrodes of the LBEs are separated by few millimetres, a huge distance compared to the size of the cells. The resistance of the solution between the electrodes, R_{Sol}, is then considered very high. For a cell adhered to the measuring electrode, the overall impedance Z_{Seal} that seals it from the counter electrode is so high that $i_1(t) >> i_2(t)$. This guarantees that the signal generated by this cell, $v_{cell}(t)$, is only captured by the measuring electrode. The capacitive effect of the electrolyte solution, C_{sol}, despite represented in the circuit, is neglectable.

The measurements with LBEs are optimized when taken in current mode, instead of the usual voltage measurement. A transimpedance amplifier can convert the small current captured by the measuring electrode, $i_1(t)$, into a considerable voltage output, $v_o(t)$, as shown in Equation 5:

$$v_o(t) = -R_F i_1(t) \tag{5}$$

where R_F is the feedback resistance of the transimpedance amplifier. The value of $i_1(t)$ can be deduced based on the equivalent circuit shown in Figure 2.2. A few considerations must be made though. First, it is not simple to model the capacitive effect of the double layer (CPE_{DL}) mathematically. It requires differential equations with derivatives and integrals of non-integer orders, which are technically challenging to solve, demanding complex numerical methods [73]. For this reason, and since the purpose of this circuit analysis is to provide an overall view of the effect of the large area on the performance of the measuring system, the capacitive effect of CPE_{DL} will be simplified to a perfect capacitor, which will be named C_{DL}. That is a suitable approximation for extracellular recordings [74], commonly used in the literature. Also, assuming $R_{CT} \gg R_{cleft}$, the time constant of the system can be approximated to $\tau \approx R_{CT}C_{DL}$. The current $i_1(t)$ can then be given by Equation 6 (full mathematical deduction in [18]).

$$i_1(t) \cong \frac{v_{cell}(t)}{R_{CT} + R_{cleft}} + \frac{dv_{cell}(t)}{dt} C_{DL}\left(1 - e^{-t/\tau}\right) \tag{6}$$

Equation 6 evidences some interesting properties of this displacement current method. It is shown that the amplitude of the current signal increases with C_{DL}. The double layer capacitance is proportional to the area of the electrode, as already mentioned. This implies that the use of large area electrodes will lead to a larger signal output when measured in current mode [48]. Also, the derivative

term $dv_{cell}(t)/dt$ forces a large displacement current through the double-layer capacitance at the rising and falling edges of the voltage signal. Consequently, the voltage oscillations are highlighted in current mode.

2.3.2 Detection of Glioma Bursts with Large Bi-Electrodes

With the LBEs it is possible to measure the cooperative fluctuations in membrane potential of cell populations. One of its prime targets are the glioma cells. There is a strong need to understand the type of activity displayed by a multicellular glioma, and what triggers it. The LBE approach was tested with a culture of rat C6 glioma cells in [20]. It is a commonly used cell line to model glioblastomas [75], the most frequent type of glioma. An example of a recorded signal is shown in Figure 2.3. The signal is shown in pA because the acquisition system favours the current detection as explained before. In the first hours of incubation, the captured signal has the appearance of background noise – region (I) in Figure 2.3.A. It is actually the sum of the residual random activity of each individual cell adhered to the electrode. The signal amplitude increases with time, region (II), and then enters in a quasi-periodic phase, region (III), as seen in more detail in Figure 2.3 (B). Because the collected signal is the superpositions of the individual responses of the cells, the quasi-periodic behaviour is the result of a cooperative and synchronized bursting phenomenon of these glioma cells.

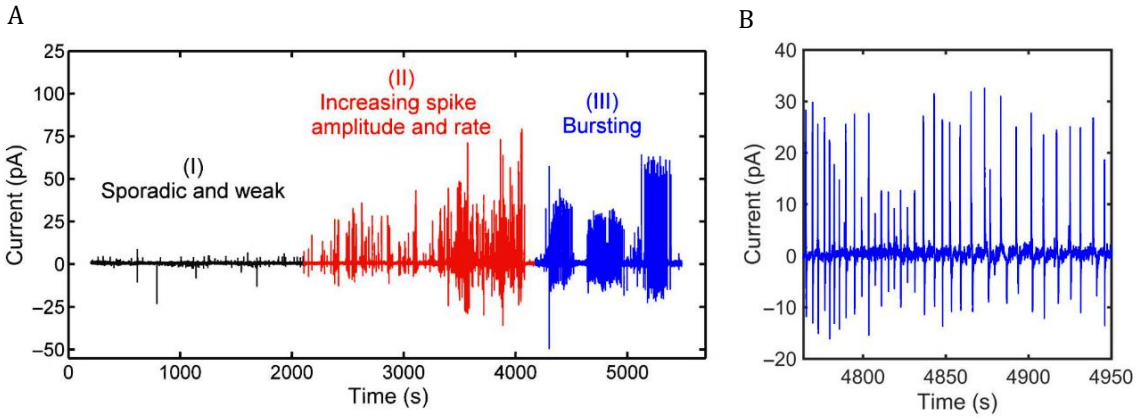

Figure 2.3. Current signal of the C6 glioma cell populations [20]: (A) Overall signal divided into three distinct activity regions; (B) Zoom-in of the bursting activity, region (III).

The electrical bursting was shown to be related with the lowering of pH, caused by the tumour metabolism itself. It was then demonstrated that the low pH enhanced the flux of Na^+ through the ASICs. The electrical activity recorded was the result of a self-induced mechanism.

This *in vitro* experiment showed that an acidic extracellular medium can induce a significant synchronized electrical activity in glioma cultures. This event is likely to occur in real gliomas because the microenvironment of tumours is strongly acidified by the release of lactic acid [76]. Many other brain pathologies such as stroke, epilepsy, Parkinson's disease, hyperalgesia, multiple sclerosis are associated with acidosis [41]. The pH-triggered electric currents detected in the glioma cell cultures may perturb the normal vesicular neurotransmitter release performed by glia cells, leading to epileptic seizures.

These conclusions are in line with a recent study that reports how brain inflammation acidosis leads to epileptic seizures in mice due to the activation of ASIC in astrocytes [77]. They showed that

epileptic seizures were significantly reduced by inhibiting the expression of ASICs in astrocytes. Even though the event that leads to an acidic microenvironment is inflammation and not the metabolism of a glial tumour, the mechanisms that induce the epileptic seizure would be analogous and, therefore, mutually corroborated by both researches. Showing that a *in vitro* glioma population can manifest self-induced bursting activity is not enough to relate it with epileptic seizures. In this sense, the results obtained in [77] with epileptic mice were very important. They show that a lower brain pH associated with inflammation caused epileptic seizures due to the abnormal activation of ASICs in astrocytes. It is then possible that these glia cells are displaying the synchronized burst activity described in [20], disturbing the normal glia-neuron communication.

With the LBE approach it was possible to monitor the activity of glioma populations for long periods of time. The results obtained with this LBE provided meaningful insights about the glioma communication, which is characterized by a synchronized and cooperative bursting activity. Further research must still be performed to link these behaviour with a possible epileptogenic mechanism. Enhanced LBEs – with a better SNR and biocompatibility – would be extremely useful for this purpose.

2.4 PEDOT:PSS and CNT as electrode coatings

The LBEs used for cell monitoring were originally implemented with gold electrodes [18]–[20]. The transducers were remarkably sensible being capable of detecting the ultra-weak cell activity. The successful proof of concept presented in the previous section justifies moving towards a more developed version of the device. There are two main improvements to aim at: better SNR ratio and better biocompatibility. As explained in the section 2.3.1, the SNR increases with an improved cell coupling and a lower interfacial impedance. Biocompatibility on the other hand is related with the physico-chemical properties of the electrode's surface, which must allow the cells to adhere and proliferate. Both criteria can be met with the use special coatings over the electrodes.

An important breakthrough on the field was the synthesis of poly(3,4-ethylenedioxythiophene): poly(styrenesulfonate) – PEDOT:PSS – a chemically stable polymer-polyelectrolyte system with promising features in terms of conductivity, stability, transparency (at low quantities, otherwise it is blue) and biocompatibility [78]–[80]. The resistivity of PEDOT:PSS varies according to the particle size, PEDOT/PSS ratio, solid content in water, etc. It can range from 5000 Ω.cm to 0.0012 Ω.cm. This polymer is prepared by oxidizing the corresponding monomers which leads to the accumulation of positive charges every three to five monomeric units [81], as shown in the molecular structure of PEDOT, in Figure 2.4.A. These positive charges work as charge carries for electric conduction.

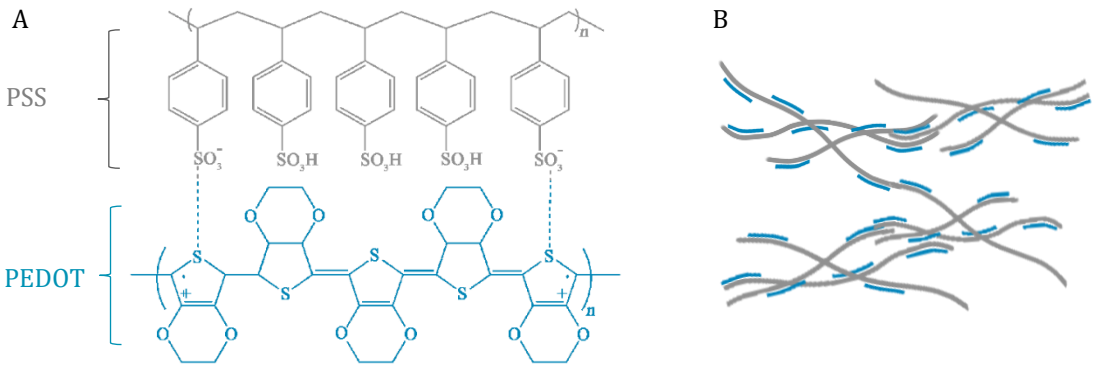

Figure 2.4. Structure of PEDOT (blue) and PSS (grey): (A) molecular composition of PEDOT:PSS; (B) polymeric matrix of PEDOT:PSS in a PEDOT rich region, called grain (separating the PEDOT grains are layers of mainly PSS)

One of the characteristic properties of this conductive polymer is its porosity. The resulting benefits are twofold. First, surface roughness is associated with a significant increase of the sensing area. As explained in section 2.3.1, a larger area increases the capacitive effect of the interfacial double layer which lowers its impedance. Secondly, a rough and porous surface provides anchoring points for the cells to adhere, reducing the cell cleft and its associated signal attenuation. The surface of PEDOT:PSS films becomes particularly rougher when immersed in solvent due to the swelling of the polymeric matrix [23], [82].

Another interesting property that makes PEDOT:PSS a suitable candidate for electrode coatings is its electronic and ionic conductivity [83]. Cell signals are propagated through ionic currents. The movement of ions into and out of the polymeric matrix (shown in Figure 2.4.B) induce PEDOT:PSS redox reactions. Unlike gold electrodes which are almost free of faradaic reactions, conductive polymers have low redox potentials which enable an easy and reversible oxidation/reduction of the ma-

terial. This way, PEDOT:PSS establishes a suitable interface in bioelectronic devices because it facilitates the translation between ionic flow and the electronic currents [81],[84],[85]. PEDOT:PSS coated electrodes show a higher SNR than the commonly used materials [86],[87] and were reported to remain chemically stable when stimulated for two weeks [86].

As for the biocompatibility, PEDOT is known to settle a stable interface with biological elements. However, the ability of cells to adhere and proliferate in this material is not fully understood yet [80]. One of the reasons may be its mechanical softness which biomimics the extracellular matrix [88], unlike the stiff metal surfaces. Despite being favourable for biocompatibility, the softness of this material is associated with a low mechanical stability. The poor adhesion of PEDOT:PPS to underlying inorganic substrates imposes a severe practical limitation [89].

The conductivity of PEDOT:PSS electrodes can even be increased with the use of dopants. One of the most used dopants for PEDOT:PSS film processing is Dimethyl Sulfoxide (DMSO). The conductivity of the increases drastically with the addition of this dopant. It was shown that at a DMSO:(PEDOT:PSS) ratio of 1:5 the conductivity increased by more than three orders of magnitude [90]. The rise in conductivity is due to the increase in grain size of PEDOT particles and the thinning of the PSS insulating barrier that naturally occurs between PEDOT grains [91], [92]. The conductivity decreases at proportions higher then 1:5 DMSO:(PEDOT:PSS) due to the increased separation between PEDOT grains. However, DMSO is cytotoxic leading to cell death at high concentrations. The lethal proportion varies according to the type of cell. Some cells can tolerate a substrate with 2% DMSO [93] while others stand until 10% [94], for instance.

PEDOT:PSS was already used to fabricate electrodes in LBEs [24]. The interfacial impedance of these electrode was three orders of magnitude lower than that of the conventional gold electrodes. This led to a lower background noise and higher sensitivity.

Composites of PEDOT:PSS and CNT have been widely studied for neurophysiological applications [95]–[97]. CTN are famous for their mechanical strength and conductivity. CNTs can be single-walled or multi-walled nanotubes, the first being composed of single graphene cylinders, and the latter having multiple concentric cylinders. The length-to-diameter ratio can reach 132,000,000:1 [98]. The introduction of this carbon allotrope in a polymeric matrix increases the mechanical resistance of the electrode coating and its surface roughness. The high conductivity of CNT improves the ionic and electronic conductivity of PEDOT:PSS composites. Similarly to the phenomena described for PEDOT:PSS films, the high surface roughness of CNT films leads to a large effective area. Recent work shows that CNT can promote cell attachment and proliferation of neurons [25], [27]. The cell attachment is facilitated by the roughness of CNT. Also, adding CNT to PEDOT:PSS lowers the overall percentage of DMSO (which is cytotoxic), while still ensuring a very conductive film.

3 Sensors

Monitoring the electric activity of glial cells is a very demanding task due to the low amplitude and frequency of their signals. It was already made possible with the use of large area electrodes and research should now be focused in improving the sensing capabilities of these devices. That is one of the main goal of the presented dissertation. The approach being studied here is the use of PEDOT:PSS and/or CNT to coat the electrodes of the device.

This chapter will be focused on the fabrication and characterization of the developed sensors. In the first section we will present the different techniques and materials used to prepare them. Section 3.2 will be dedicated to the characterization of the electrode's surface, both in terms of its surficial topography and electrochemical properties. We will finalize this chapter with section 3.3 where we summarize the main conclusions and suggest the future work regarding the sensor's fabrication.

3.1 Sensors Fabrication

This section will be focused on the fabrication protocol of the devices. This experimental procedure was conceived iteratively, in response to the limitations and difficulties encountered in the development process. Ideally the implemented protocol should be easily reproduced and, if possible, enable the mass production of the devices. Thus, the initial plan was to ink-jet print the polymer coatings on PCB devices identical to the one shown in Figure 3.1.A. Ink-jet printing is a cheap, fast and reproductible way of coating electrodes with polymer films [99]. It has been widely used to coat electrodes and MEAs [100]–[104]. Recently, it was applied to coat LBEs with PEDOT:PSS [24]. However, it was not possible to conclude the development of the sensors with this technique due to technical problems with printer. A new method was implemented that consisted in manually drop casting the polymer over the electrodes, as described in 3.1.3.

Having the sensor in a PCB based technology would also bring several practical and commercial advantages: the devices could be standardized and mass produced and it would be easy to incorporate new electronic components to build more complex acquisition systems. These devices, shown in Figure 3.1.B, have gold electrodes plated over copper on a FR4 substrate (polymer that constitutes the base of the PCB). The sensors were manually coated with PEDOT:PSS and CNT composites with a procedure similar to the one described below. An example of the resulting devices is shown in Figure 3.1.B. However, these coated sensors were not biocompatible. It was known that uncoated electrodes were toxic to the cells due to the copper under the gold electrodes. Apparently, the polymer coating over the electrode was not enough to insulate the cell culture from the copper. As a result, the measurements made with the coated PCB devices led to the death of the entire cell population.

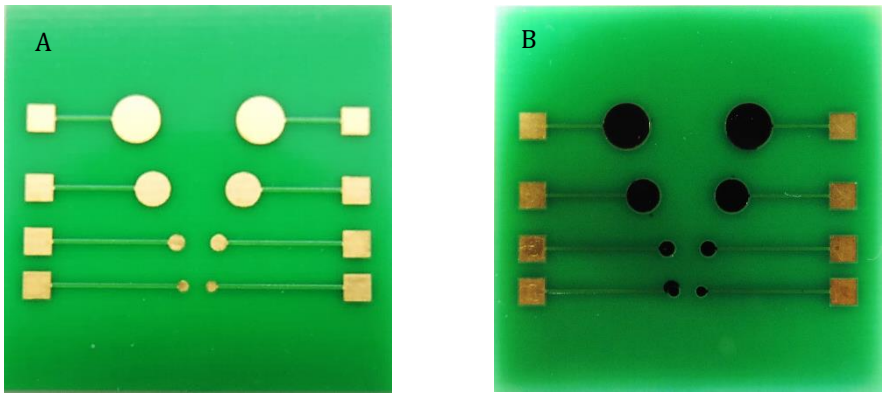

Figure 3.1. The PCB devices developed: A) device with the exposed gold electrodes; B) device with PEDOT:PSS coated electrodes;

The devices fabricated in the next development iteration had a glass substrate over which the gold electrodes were evaporated (Figure 3.2.A) and coated with the polymer composites (Figure 3.2.B). The following sub-sections will describe how these steps were performed and why. They will be structured as follows: 1) fabrication of the glass substrate with the gold electrodes; 2) preparation of the coating mixtures; 3) drop-casting the mixtures over the electrodes.

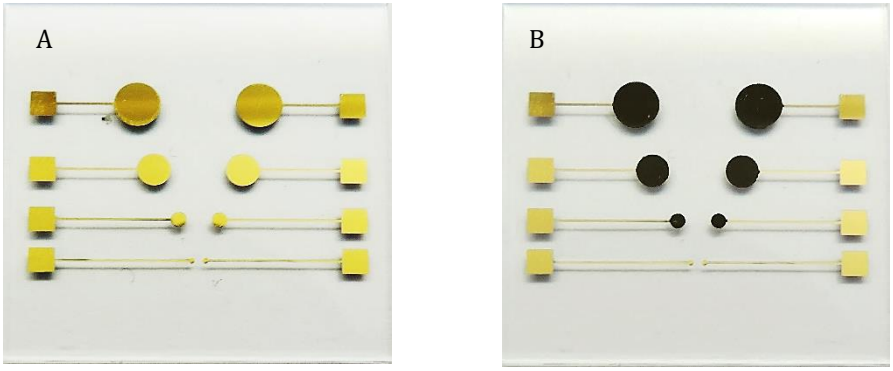

Figure 3.2. The final devices developed: A) device with the exposed gold electrodes; B) device with coated electrodes.

3.1.1 Evaporation of the Gold Electrodes

The device fabrication begins with the evaporation of the gold electrodes over a glass substrate. The result of this first step is shown in Figure 3.2.A. Each sensor has 4 pairs of electrodes with different dimensions. The areas are, approximately, 10 mm^2, 6 mm^2, 2 mm^2, 1 mm^2. This way it is possible to test the effect of the area on the performance of the electrodes.

The glass substrate and the source materials – chromium and gold – need to be rigorously cleaned before the performing the thermal evaporation. The gold and chromium were cleaned in ultrasonic bath with acetone for 10 min. It is particularly important to have a very well cleaned glass substrate. The substrate was scrubbed with water and soap for 2 min to remove residual dirt and dust particles, followed by rinsing with ultrapure water (Milli-Q water). It was sonicated in acetone for 5 min, and then in isopropanol for 5 min. The ultrasonic bath helps to degas the substrate and remove residual particles and water. The substrate was dried in high pressure nitrogen to evaporate the isopropanol.

The materials were then properly placed in a vacuum chamber to begin the thermal evaporation. First, the chromium is heated and vaporized. Chromium particles travel directly to the glass substrate placed above. A mask with the shape of the electrodes covers the glass. When the vaporized chromium particles reach the masked glass, they condense with the electrode's shape over the substrate. The chromium coating had a thickness of about 10 nm and was meant to work as an adhesion layer for the gold. The gold was then vaporized over the glass, analogously to the chromium. The gold layer had a thickness of 50 nm.

3.1.2 Preparation of the Coating Mixtures

The PEDOT:PSS used was the aqueous dispersion PH1000 (Clevios). It was mixed with 5% of DMSO (Sigma-Aldrich) which increases the conductivity to, at least, 850 S/cm, as stated by the provider. The CNT dispersion used was the CNT ink Nink-1000 (NanoLab), an aqueous suspension of carboxyl functionalized multi-walled nanotubes (15 nm diameter and 1-5 μm length).

Three coating mixtures were prepared: one with PEDOT:PSS/DMSO (which from now on, we will refer to as simply PEDOT:PSS), one with CNT, and another with a mixture of both (50% V/V). To each of these dispersions was added a small portion of (3-glycidyloxypropyl) trimethoxysilane

(GOPS) in the proportion 1:100. The mixtures were mixed in a vortex mixer for 30 seconds. GOPS lowers the conductivity of the mixture but the adherence and mechanical stability of the coatings were significantly improved, in line with what was reported in literature [98]. The initial iterations of the protocol did not include GOPS and the resulting devices had poorly adhered coatings which easily detached in the sterilization procedure that precedes the cell culturing.

3.1.3 Drop-Casting the Coatings

The final step of the device fabrication is drop-casting the prepared mixtures over the gold electrodes to create the intended film. Drop-casting is a very simple, quick and accessible procedure to create thin films on small substrates. As the name suggests, it consist in dropping a established volume of a solution/dispersion over a substrate and waiting for the medium to evaporate.

The glass substrate with the gold electrodes must be properly cleaned before drop-casting the dispersions. That was achieved by scrubbing the surface with isopropanol, followed by UV ozone cleaning for 10 min. It was used the UV/Ozone ProCleaner from BioForce Nanosciences. The ozone breaks down the surface contaminants into volatile compounds which evaporate from the surface. It also has a very useful secondary effect: it increases the hydrophilicity of the substrate's surface, making it easier for the drop to adhere and spread over the electrode.

Once the substrate was cleaned, the dispersions could be directly drop-casted over the electrodes with a micropipette. This procedure had two main variables that had to be empirically optimized: the drop volume and the drying temperature. The drop volume determines the thickness of the film and how easy it is to spread the dispersion. Large drops overflow from the electrodes into the glass substrate and very small drops may be difficult to spread and form a continuous film. The drop volume establish was 0.25 $\mu l/mm^2$. As seen in Figure 6.B, the smaller electrode was not coated because the volume required was lower than the limit of the micropipette and using larger volumes would easily cause overflow. The drying temperature has a significant impact on the conductivity of the PEDOT:PSS. The activation of charge carriers and the crystallinity order of the polymer increase with heating, reaching a maximum at a temperature between 120 and 140 °C [105]. The effect of temperature in the CNT structure is only relevant for very high temperatures. The coatings were dried at 140 °C for 1 h.

3.2 Sensors Characterization

The three types of sensors fabricated – PEDOT:PSS, PEDOT:PSS with CNT, and CNT – were characterized in terms of their surface topography and electrophysiological properties. The surface roughness was accessed by Atomic Force Microscopy (AFM) – section 3.2.1. The electrophysiological study was focused on the analysis of the interface electrode/electrolyte, based on the results of Electrochemical Impedance Spectroscopy (EIS) – section 3.2.2.

3.2.1 Atomic Force Microscopy

The electrode coatings are expected to increase the sensing area due to the high surficial roughness acquired. AFM measurements were taken to map the surface of the different types of electrodes. The resulting images are compiled in Figure 3.3, for the gold electrodes and for the ones coated with PEDOT:PSS, PEDOT:PSS/CNT, and CNT. The average roughness of the different surfaces was calculated based on the AFM results using the imaging analysis software Gwyddion. The average roughness corresponds to the mean value of height irregularities in relation to the average height. The values obtained for the different coatings are represented in Figure 3.4. These were calculated based on the 1 μm AFM images shown in Figure 3.3.

The images of the gold electrodes reveal a flat surface. In Figure 3.3.A there is an interval of 65 nm between the lowest and the highest points of the image, but these are respectively associated with scratches and dirty particles over the electrode. The lack of texture on the rest of the electrode is evidenced by the colour homogeneity of Figures 3.3.A and 3.3.B. The mean surface roughness for the gold electrode is 1.30 nm (Figure 3.4).

The surface of the PEDOT:PSS coated electrodes is shown in Figure 3.3.C and 3.3.D. The texture of these coatings is manifested in two different levels of magnitude. At a larger scale, the surface exhibits large agglomerations of PEDOT:PSS, more than 100 nm high. These structures can be seen in Figure 3.3.C and are found all over the electrode. In a smaller scale, the surface texture is determined by the polymeric filaments of PEDOT:PSS, as seen in Figure 3.3.D. That is the most prevalent texture of the coating. As represented in Figure 3.4, the mean roughness of this electrode has an amplitude of 2.20 nm. As expected the sensing area is increased with the addition of the polymeric coating.

The addiction of the CNT ink to the PEDOT:PSS dispersion originated a considerably rougher electrode coating as evidenced in Figure 3.3.E. The PEDOT:PSS agglomerates seen in Figure 3.3.C are still visible here. In the zoomed-in image, Figure 3.3.F, it can be seen that the structures formed by the combination of these two materials are much larger and higher than the PEDOT:PSS filaments. The mean roughness associated with this image is 8.48 nm (Figure 8). The addition of CNT to the coating led to a considerably rougher film.

The electrodes coated with only CNT have the highest surface roughness. The texture amplitude reaches hundreds of nanometres and the individual nanotubes can be easily identified in both images. The dimensions of the nanotubes seen in Figure 3.3.H are coherent with what was expected for the ink used, having a thickness in the dozens of nanometres range and a length in the micrometre range. The mean roughness obtained for the image of Figure 3.3.H is 24.98 nm.

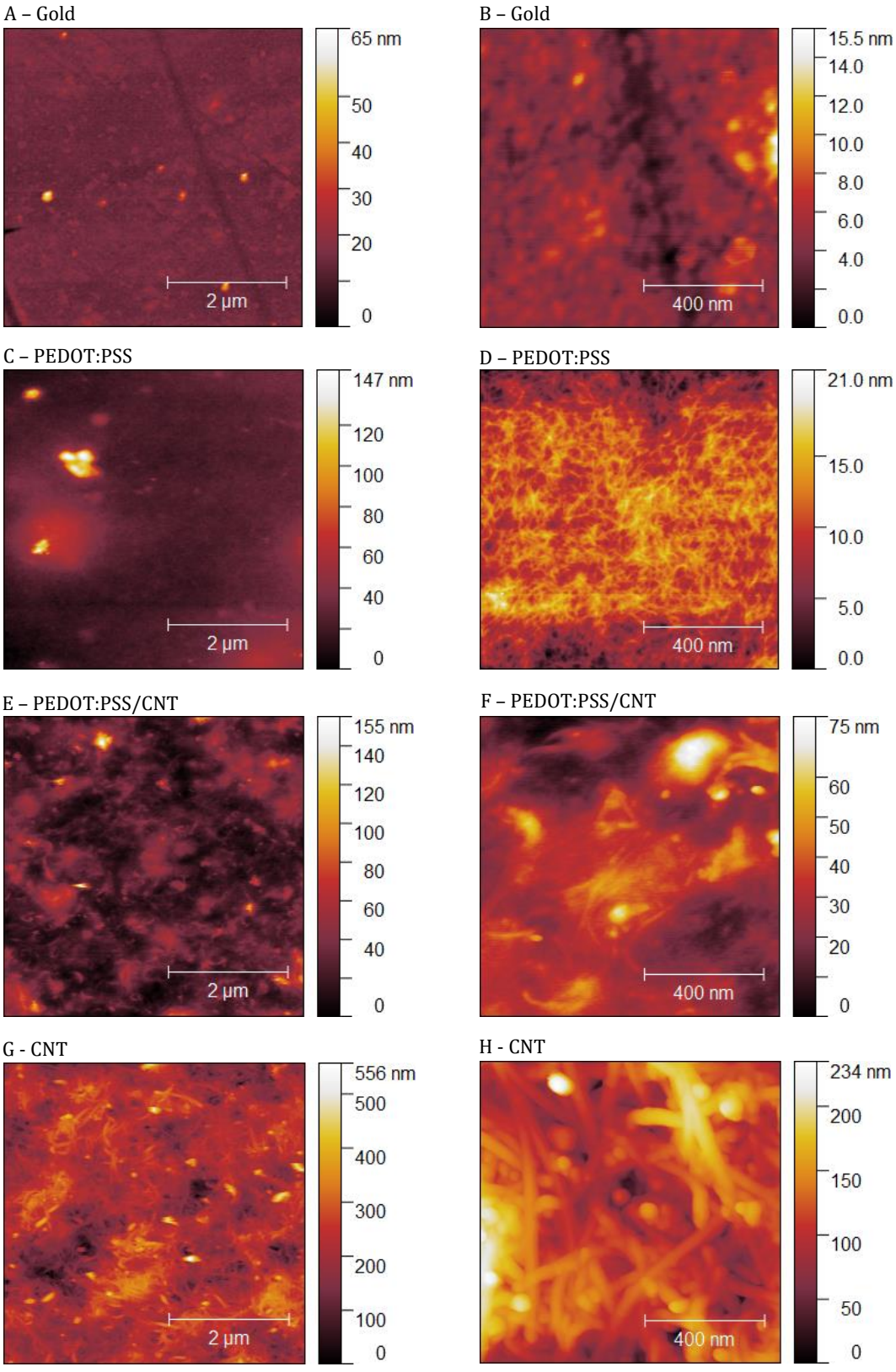

Figure 3.3. AFM images of: A) and B) gold electrodes; C) and D) electrodes coated with PEDOT:PSS; E) and F) electrodes coated with PEDOT:PSS and CNT; G) and H) electrodes coated with CNT. The images on the left are 5 µm wide and the right images are 1 µm wide.

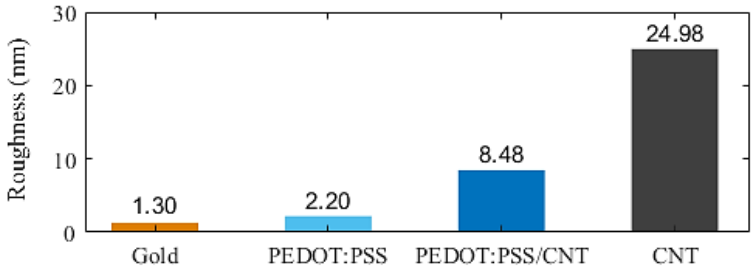

Figure 3.4. Mean roughness of the different electrodes for the 1 µm AFM images.

So, as expected, the surficial roughness of the fabricated sensors is significantly larger than that of the uncoated gold electrodes. Also, the CNT create a surficial texture with a much higher amplitude than the PEDOT:PSS. Its surficial roughness is approximately 10 times larger than in PEDOT:PSS. As already mentioned in section 2.4, the benefits of a high surface roughness are twofold: it is expected to lower the interfacial impedance leading to a lower background noise and increase the cell coupling lowering the signal attenuation that characterises the extracellular recordings. The first of these two features were evaluated with the Electrochemical Impedance Spectroscopy, as explained in the next section.

3.2.2 Electrochemical Impedance Spectroscopy

As explained in 2.2, the interfacial impedance of the electrodes should be minimized to reduce the background noise. Also, in the LBE equivalent circuit analysis done in section 2.3.1 it was explained how important it is to have a high double layer capacitance (CPE_{DL} in Figure 2.2), particularly when performing measurements in current mode. The impedance is calculated by applying an AC potential over the electrodes and measuring the resulting current. The frequency of the AC signal changes within a specified range to characterize the behaviour of the electrodes over a broad frequency spectrum. The measurements were made with a Solatron 1260 Impedance Analyzer, with a very precise needles system as shown in Figure 3.5.A. Simpler acquisition setups led to imprecise results due to inherent background noise.

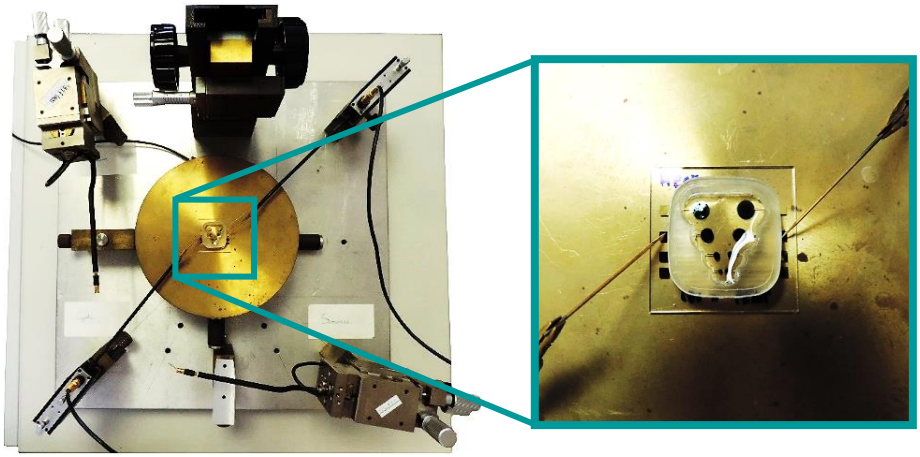

Figure 3.5. Experimental setup for the impedance measurements: A) very sensible needle acquisition system; B) detail evidencing the sensor and the measuring needles.

The electrolyte is placed inside a compartment to cover the electrodes without leakage. It can be seen in Figure 3.5.B that the internal shape of this compartment surrounds the electrodes. This aims to minimize the measuring effect of the gold lines that connect the circular electrodes to the quadrangular connectors outside the compartment. Thus, the measuring area is mainly the electrode's surface. Otherwise, the full surficial area of the line would have an impact on the measurements, especially for the smaller electrodes, and make the comparisons between the electrode areas imprecise.

The main variables that influence the electrode/electrolyte impedance are the area, roughness and material of the electrode's surface, and the ion concentration of the electrolyte. The electrolyte used is KCl diluted in water with a concentration of 100 mM. This concentration was chosen because it is approximately the ion concentration of the cell medium used later (and the idea of this analysis is to access the electrochemical properties of the sensors in those conditions). The effect of the electrode's area on the interfacial impedance is evidenced in Figure 3.6. The data shown correspond to the measurements taken for the gold electrodes (without any PEDOT:PSS or CNT coatings).

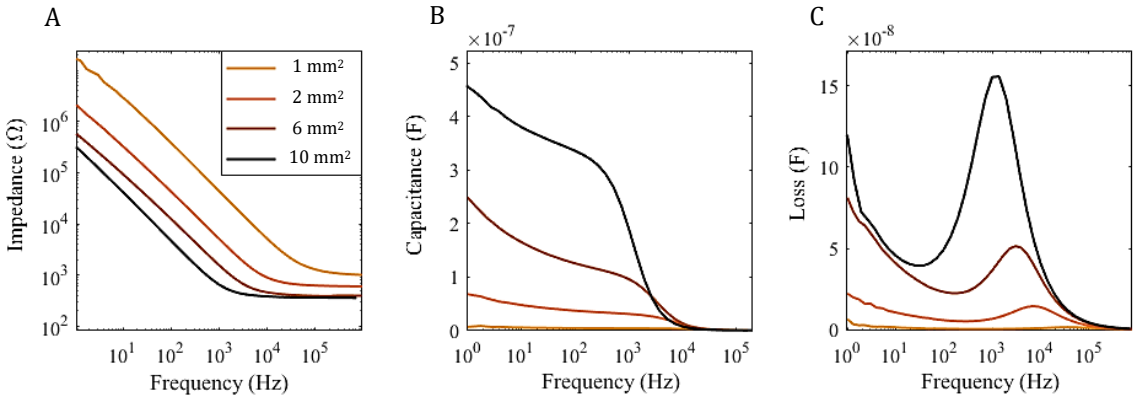

Figure 3.6. EIS results for the gold electrodes with different areas: A) modulus of the measured impedance; B) real part of the complex capacitance extracted; C) extracted dielectric loss (imaginary part of the complex capacitance). The legend shown in A) is also applied for B) and C).

The area/impedance relation verified for the gold electrodes also occurs for the coated sensors. However, the gold surface is more electrochemically uniform and, therefore, generates more uniform impedance curves. For this reason, it was the sensor chosen to explain the shape of the different curves and its relation with the area. Later we analyse the effect of the different coatings.

To understand the meaning of the presented graphs it is important to be aware of the electrical model considered for the electrode-electrolyte system. In Figure 2.2 we showed the electrical model of the electrodes when in contact with the cells. In the impedance measurements, however, the system is composed by only the electrodes and the electrolyte. Therefore, its equivalent circuit consists only of the parallel RC of the interface in series with the parallel RC of the electrolyte, as illustrated in Figure 3.7. The electrode/electrolyte interface is modelled by the charge transfer resistance R_{CT} and double layer capacitance CPE_{DL}. The bulk electrolyte is modelled by its resistance R_{sol} and capacitance C_{sol}, the latter being usually neglected due to its low value.

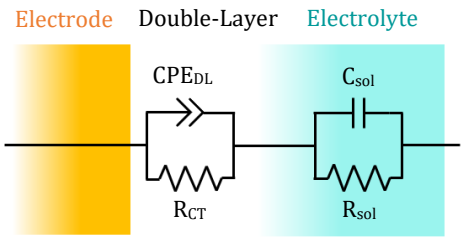

Figure 3.7. Equivalent circuit model of the system electrode-electrolyte

With this in mind, we can now proceed to the interpretation of the different curves presented in Figure 3.6. The impedance measured for the four pairs of gold electrodes is shown in Figure 3.6.A. All the curves have a similar shape – the impedance decreases linearly with an increasing frequency and becomes constant beyond a certain point. The impedance at low frequencies is determined mainly by the charge transfer resistance R_{CT} and the double-layer capacitance CPE_{DL} of the electrode's surface. The impedance of the double-layer, Z_{CPE}, decreases with an increasing frequency, as evidenced by the Equation 4 in section 2.3.1. So, as verified in Figure 3.6.A, at low frequencies (where the double-layer has a critical influence) the overall impedance decreases with increased frequency. As explained before, a larger area confers a lower interfacial impedance due to the increased capacitive effect of the double-layer. This is also evidenced in the Figure 3.6.A, where the larger electrodes have a lower impedance at low frequencies.

Increasing the frequency will eventually make the double-layer capacitance short-circuit the parallel RC of the electrode surface. Beyond this point, the overall impedance becomes independent of the frequency, since it is only determined by the in-series electrolyte resistance, R_{sol} (considering C_{sol} neglectable). This frequency independent impedance decreases with the electrode area since the R_{sol} is expressed by:

$$R_{sol} = \frac{\rho}{4r} \tag{7}$$

where ρ is the resistivity of the solution and r is the radius of the electrode. So, a larger electrode has a lower interfacial impedance at high frequencies as well.

The capacitive effect of the system is mainly due to the double-layer, since the capacitance of the electrolyte is neglectable. Its ability to store charge changes with frequency and, therefore, the capacitance is represented as a complex number. The real and imaginary parts of the capacitance can be extracted from the measured impedance according to Equations 8 and 9 [106]:

$$C'(\omega) = \frac{-Z''(\omega)}{\omega|Z(\omega)|^2} \tag{8}$$

$$C''(\omega) = \frac{-Z'(\omega)}{\omega|Z(\omega)|^2} \tag{9}$$

where $C'(\omega)$ and $C''(\omega)$ are the real and imaginary part of capacitance, $Z'(\omega)$ and $Z''(\omega)$ are the real and imaginary part of the impedance, and $|Z(\omega)|$ is the modulus of the impedance. The modulus of the impedance is measured directly on the EIS. The $Z'(\omega)$ and $Z''(\omega)$ are calculated considering this modulus and the correspondent phase angle for each frequency, also determined in EIS. The resulting $C'(\omega)$ is plotted in Figure 3.6.B and $C''(\omega)$ – here mentioned as Loss – is plotted in Figure 3.6.C.

The capacitance curves of Figure 3.6.B are characterized by two different regions. At high frequencies the capacitance of the system is almost null. The capacitive components of the equivalent circuit are short-circuited, and so the current is transmitted without the highly resistive faradaic reactions, associated with R_{CT} – the resulting impedance is minimum. At low frequencies, the double-layer exerts its capacitive effect (we are neglecting the electrolyte capacitance). As a result, the capacitance of the system increases. The curves of Figure 3.6.B evidence a relevant property of the double-layer: at low frequencies, the capacitance increases with a decreasing frequency. This means that the ability of the double-layer to store charge increases as the frequency lowers. Such event does not occur in ideal capacitors, where the capacitance is constant at low frequencies. This is the reason why the double-layer is modelled by a constant-phase element, CPE, and not a capacitor. The CPE behaviour is due to a dispersion of time constants of the coatings [71]. The slope of this region of the curve is associated with the parameter *n* of Equation 4. The value of *n* is lower for curves with a high slope, making the CPE_{DL} diverge from an ideal capacitor (which has $n = 1$).

As expected, the double-layer capacitance increases with the surface area, just like the capacitance of a capacitor increases with the area of its plates. A higher capacitance leads to a lower impedance because more current can be transferred via non-faradaic reactions. This explains why the larger electrodes have a lower impedance. At a frequency of about 10^3 to 10^4 Hz, there is a sudden transition between the two regions of the curve. At this frequency there is a change in the permittivity (ability to store charge) of the double-layer. This phenomenon is not instantaneous, occurring with a certain drag or hysteresis, known as dielectric relaxation. It is associated with the depolarization of the double-layer and occurs when the frequency of the induced current is higher than the rate of polarization of the double-layer. Beyond this frequency, the so-called relaxation frequency, the double-layer behaves as a short-circuited capacitor, having no impedance. A low relaxation frequency is then desirable, because it means that the double-layer is highly conductive at lower frequencies.

The relaxation frequency of the different electrodes can be easily identified in Figure 3.6.C, as explained bellow. The curves shown correspond to the imaginary part of the capacitance which represent the energy dissipation as a function of frequency. This dissipation effect is referred to as Dielectric Loss and reaches its maximum value at the relaxation frequency. The peak of the Loss curve shifts to lower frequencies as the area increases, meaning that a larger area lowers the relaxation frequency. This explains why the impedance curves shown in Figure 3.6.A seem to shift to the left as the area increases – a lower relaxation frequency means that the double-layer is still unpolarizable at lower frequencies, behaving as a short circuit. Also, the loss increases with the electrode area, as would be expected since the energy dissipation occurs through the electrode's surface.

The main goal of the EIS was to evaluate the effect of the different coatings. Now that it is clear how the curves of Impedance, Capacitance and Loss are shaped, we can proceed to the analysis of the EIS results obtained for the coated sensors. Figure 3.8 shows the three curves presented before, now for the sensors coated with PEDOT:PSS, PEDOT:PSS/CNT and CNT, and the uncoated gold electrodes. We will not focus on the effect of the area for each coated sensor because its influence on the shape of the curves is similar to the one verified in the gold electrodes (described above). The data presented in Figure 3.8 was extracted from the 6 mm^2 electrodes, again at with an electrolyte concentration of 100 mM. This was the area chosen because it provided the most uniform results for the

coated sensors. Before starting the analysis, it is important to note that the frequency range used for the coated sensors is different than the one used for the uncoated gold electrodes. The spectrum of frequencies used in EIS needs to adequality frame the regions of interest of the curves by centring the relaxation frequency (which is much lower for the coated sensor).

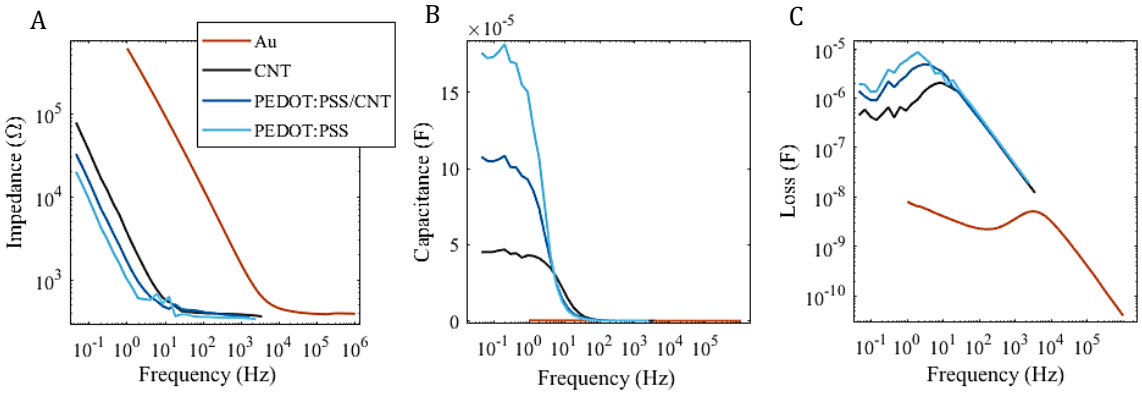

Figure 3.8. EIS results for the uncoated gold electrodes (orange) and sensors coated with PEDOT:PSS (light blue), PEDOT:PSS/CNT (dark blue) and CNT (black): A) modulus of the measured impedance; B) real part of the complex capacitance extracted; C) extracted dielectric loss (imaginary part of the complex capacitance). The legend shown in A) is also applied to B) and C)

The results presented in Figure 12 evidence a clear improvement of the electrochemical properties of the fabricated sensors when compared to the bare gold electrodes. First, the impedance values are significantly lower (Figure 11.A). In the range of frequencies expected for the cells signals – approximately between 10^0 and 10^1 Hz – the impedance is about three orders of magnitude lower for the coated electrodes. This is expected to reduce the background noise of the recordings, as already explained. It can also be seen that the PEDOT:PSS sensor has an apparently noisy impedance curve, particularly at the relaxation frequency region. However, these irregularities are not due to measuring noise because the shape was consistent in repeated recordings. This phenomenon was also found in other coated sensors, for different electrode areas. Its origin is not understood yet, but it may be related with the surface irregularities that lead to non-uniform time constant dispersions of the coating. Note also that, at high frequencies, the modulus of the impedance is practically the same for the four sensors. That happens because, at these frequencies, the predominant source of impedance is the resistance of the solution, given by Equation 7. This value depends only on the conductivity of the electrolyte and the geometrical area of the sensors, which is the same (6 mm^2, in this case).

Figures 3.8.B and C illustrate some of the factors that lead to such a low impedance for the coated electrodes. The maximum capacitance for these sensors is more than two orders of magnitude higher than that of the uncoated electrodes (the data of the gold electrodes cannot be properly visualized in Figure 3.8.B due to its low amplitude, but it is the same curve of Figure 3.6.B for the area 6 mm^2). The high capacitance is explained by the increased effective area conferred by the rough surface of these coatings. However, the effective area is not the only factor contributing to the capacitance. In fact, Figure 3.8.B shows that the PEDOT:PSS sensor has the highest capacitance even though the AFM images reveal that the CTN sensor has a rougher surface. The real part of the capacitance is also increased if there is a longer ion penetration depth in the matrix of the coating [106]. This phenomenon is likely to be more intense for the polymeric matrix of PEDOT:PSS, promoting a more effective charge storage at low frequencies than the CNT.

The coated sensors manifest their lowest impedance until very low frequencies (below 10 Hz). This feature is also evidenced in Figure 3.8.C, where the maximum of the loss curve corresponds to the relaxation frequency, as already explained. The Y axis of the graph is presented in logarithmic scale so that the peak of the gold electrodes can be identified and compared to the peaks of the coated devices. The relaxation frequency of the fabricated sensors is more than three orders of magnitude lower, meaning that the double-layer is fully conductive at much lower frequencies.

3.2.3 Fitting of the Impedance Parameters

The experimental impedance data was iteratively fitted to the equivalent circuit model using the Equations 10 and 11, which correspond to the real and imaginary part of the impedance for the circuit of Figure 3.7. This way it is possible to extract the values of the different elements of the modelled circuit – CPE_{DL}, R_{CT}, R_{sol}. According to Equation 4, CPE_{DL} is described by Q, related with the magnitude of the capacitive effect, and n, which translates its resemblance with an ideal capacitor. The solution capacitance, C_{sol}, is disregarded in this analysis due to its neglectable magnitude.

$$Z' = R_{sol} + R_{CT}\left(\frac{1 + R_{CT}Q\omega^n\cos(n\pi/2)}{1 + (R_{CT}Q\omega^n)^2 + 2\,R_{CT}Q\omega^n\cos(n\pi/2)}\right) \tag{10}$$

$$Z'' = R_{sol} + R_{CT}\left(\frac{{R_{CT}}^2Q\omega^n\sin(n\pi/2)}{1 + (R_{CT}Q\omega^n)^2 + 2\,R_{CT}Q\omega^n\cos(n\pi/2)}\right) \tag{11}$$

The values of Q, n, R_{CT} and R_{sol} extracted for the impedance curves of Figure 3.8 are represented in the bars diagram of Figure 3.9. For the sake of representation simplicity, PEDOT:PSS is referred to as PEDOT in the sensor labels of Figure 3.9.

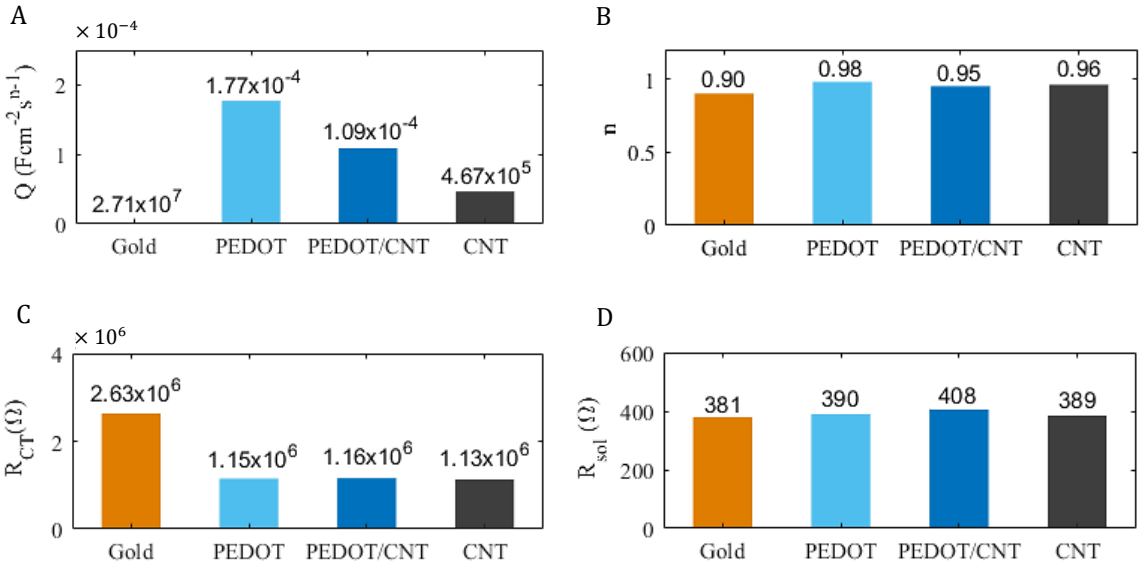

Figure 3.9. Circuit parameters extracted by fitting the experimental impedance data to Equations 10 and 11. The results were extracted from the impedance data shown in Figure 3.8 (6 mm² electrodes at 100 mM).

The effect of the different coatings on the parameters of the modelled circuit can be easily compared with the bars diagrams shown. Figure 3.9.A represents the values extracted for *Q*. The results obtained are in line with the capacitance curves presented before – the coatings significantly improved the capacitance of the electrodes, being better for the PEDOT:PSS sensor, and decreasing with the addiction of CNT.

The *n* values shown in Figure 3.9.B are close to 1. This was expected since the double-layer behaves like a (non-ideal) capacitor. There is a slight increase of *n* for the coated sensors. This was not expected because *n* was reported to decrease for irregular and inhomogeneous surfaces and the AFM results clearly show that the coated electrodes are rougher than the gold ones. This apparent contradiction may be due to the range of frequencies used to measure the impedance of the coated electrodes which led to a miscalculated value of *n* for these sensors. As explained before, *n* decreases with an increasing slope of the capacitance curves at the low frequency region. Indeed, the gold electrodes curves (Figure 3.6.B) seem to have a higher slope than the curves of the coated electrodes, which look flat for low frequencies (Figure 11.B). However, this may be due to the fact that, for the gold sensors, it was possible to use frequencies until three orders of magnitude below the relaxation frequency, where the larger increase in slope can be properly detected. On the other hand, the relaxation frequency of the coated electrodes was so low that it was not feasible to scan the electrodes at frequencies three orders of magnitude below this point. So, it is likely that an increase in the slope of these sensors would only be detected at lower frequencies than the ones used, which would then be manifested in a lower *n* value.

As explained in section 2.3.1, R_{CT} is associated with the charge transference resistance between the electrode and electrolyte through redox reactions. As expected, the value of R_{CT} is lower for the coated electrodes. According to the explanation given in section 2.4, the low redox potentials of PEDOT:PSS ensure an easier charge transference between the electrodes and electrolyte. The addition of CNT was also reported to enhance the ionic and electronic conductivity of the coatings. The R_{CT} does not change significantly with the type of coating. So, the impedance differences found for these sensors must be due to their distinct capacitive capabilities. Finally, the value of R_{sol} is naturally very similar for the four sensors since it is only dependent of the electrolyte and the radius of the electrode used. Eventual variations may result from a non-ideal fitting to the experimental data.

3.3 Conclusion

Three types of LBEs were fabricated with the protocol conceived. These were composed by a glass substrate with evaporated gold electrodes, and a drop-casted film of either PEDOT:PSS, PEDOT:PSS and CNT, or CNT. The surface of the sensors was then characterized in terms of its topography and electrochemical properties. All the devices developed presented a significant improvement compared to the conventional gold electrodes. The AFM images showed that the CNT coated sensors had the roughest surface. This should be an indicator of having the best electrochemical properties since the larger effective area leads to a lower interfacial impedance due to the increased capacitance. However, the EIS measurements showed that the PEDOT:PSS coated bio-sensors had a significantly higher capacitance, and, therefore, a lower impedance when compared to the rough CNT electrodes. This may be an evidence of the outstanding capacitive properties of PEDOT:PSS films. The experimental EIS data was then fitted to the impedance equations of the circuit model considered. The results unambiguously showed that the low impedance of PEDOT:PSS is due to its high capacitance, since the R_{CT} is similar for PEDOT:PSS and CNT. To the best of our knowledge this is the first time that the surface properties of LBEs coated with PEDOT:PSS and/or CNT are analysed in such depth.

The results from EIS show that the PEDOT:PSS sensor has the best the electrochemical properties. This does not mean, however, that it is the best sensor for the cell recordings. There are other important parameters that cannot be accessed by EIS, like the cell adhesion (which reduces the cell cleft), the biocompatibility/non-cytotoxicity, mechanical stability. These three parameters are expected to be improved with the addiction of CNT because: 1) its rough surface should ensure a better cell adhesion reducing the signal attenuation of the extracellular recording; 2) its addition decreases the overall amount of DMSO in the coating, making it less cytotoxic; 3) its higher mechanical stiffness creates a more resistant coating. So, the PEDOT:PSS/CNT composite constitutes a promising sensor coating, taking advantage the benefits of both materials. For this reason, this was the device chosen for the cell measurements presented in the next chapter.

The future work related with the sensors should be focused on improving the devices to a PCB based technology with a reproducible way of coating the electrodes. The main limitation found for the PCB substrates was its cytotoxicity, induced by the copper underlying the gold electrodes. This could be solved by covering the borders of the gold electrodes with the polymeric layer of FR4, which is biocompatible. Ink-jet printing is probably the most practical and efficient method to reproductively coat the electrodes in large scale. The next stage of development should then focus on retaking this methodology.

4 Software Development: Signal Acquisition and Analysis

The developed sensors will be used to perform long time recordings of glioma populations. The signals collected will provide insightful information about the cooperative behaviour of these cells. However, the cells activity can only be studied if the measured data is stored for future analysis. This requires an acquisition program that establishes an interface between the user and the measuring system. Once the signals are stored, they can be submitted to any sort of analysis. The bursting activity of the cell populations can be characterized by three main parameters: the spiking frequency and the amplitude and width of the spikes. The measurements may contain hours or even days of recorded data, making it unfeasible to extract these parameters through a direct visual inspection. For this reason, it is mandatory to have an efficient tool that provides a more direct way analysing the signals. This tool should be able to deconvolute the entire signal into its fundamental spike parameters – spiking frequency, amplitude and width – and translate how these change with time. The software developed accomplishes this with 3D representations that evidence how the histograms of each parameter changes over time.

The software tools developed are already being used by the scientists at the University of Bath, UK. Section 4.1 will be focused on the software developed for signal acquisition. Section 4.2 will explain the concept and algorithm behind the signal analysis software. We conclude this chapter in section 4.3 and propose the future work regarding the software development.

4.1 Signal Acquisition Software

The acquisition program is the interface between the acquisition hardware, the computer and the user. It was developed in Matlab and was conceived into an easy to use platform which enables the recording of data from up to four channels. This sub-chapter will describe how the program works and how it is used. Section 4.1.1 briefly explains the communication principle established between the computer and the dynamic signal analyser. In the section 4.1.2, we make a detailed explanation of the architecture of the program, along with a description of how it is used.

4.1.1 Controller-Device Communication

As explained in detail in section 5.1, the measuring unit of the acquisition system in the Dynamic Signal Analyser Agilent 35670A, an ultra-sensitive device capable of recording up to four channels. The computer program must communicate with this device to control the recording settings (such as the sampling rate and number of channels being read) and extract the measured data. In this context, the computer is known as the "controller" and the signal analyser is the "device". The controller-device communication is made via a GPIB-USB-HS interface. Different types of information can be shared via GPIB, but we will only focus on the Commands and Data Units.

Commands are strings sent from the controller to make the device perform a certain task, such as taking a measurement or configuring an internal setting. There are standard GPIB commands which can be interpreted by any device, however, almost all the commands used in the developed software are specific to the Agilent 35670A (available on the GPIB Programming Manual of the device). This means that the acquisition program can only be used with this equipment.

Data Units are used to share information between the controller and the device, such as the acquired data, which is sent from the device to the controller. The data measured by the Agilent 35670A is sent to the computer in blocks (as opposed to point-to-point). This means that the data of each block is only addressed to the output buffer after acquiring all the points of that block. So, while a new block is being read, the previous is temporarily kept in the output buffer. During this time, the controller can send a Command asking for the data stored in the buffer of the device.

The interface between the computer and the signal analyser was implemented with Matlab. There are no Matlab *plug-ins* available to control the Agilent 35670A. These would make the controller-device communication easier from the point of view of the developer, allowing the programming to occur in a higher level. So, here, each device setting, data formatting, acquisition configuration, action command, etc., had to be individually sent to the device, in the correct format and order.

4.1.2 Program Structure and User-Interface

The acquisition software is meant to work for hours or days, non-stop. Also, it was developed for any scientist that may need to use the measuring system available (described in section 5.1). Therefore, it needs to be easy to use and safe from any errors that may compromise the recording. It is essential to implement an adequate software architecture in order to achieve a high performance and avoid unexpected errors, especially due to the absence of Matlab *plug-ins* to work with the 35670A. The program is structured as a state machine because it is a simple and effective way to organize the code.

It guarantees that the different internal functions (and associated elements of the interface) are confined to a well-defined stage of the usage cycle of the program. The state machine developed has four states: *Disconnected*, *Stopped*, *Recording* and *Paused*. The transitions between states are illustrated in Figure 4.1. Each state will be described below, both in terms of its internal functioning and the associated user-interface elements.

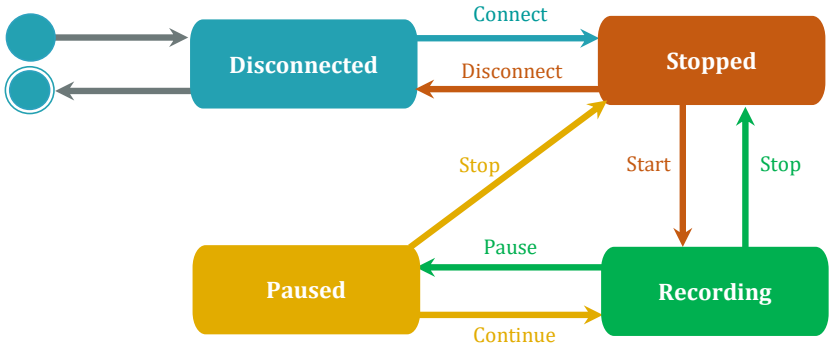

Figure 4.1. Connectivity of the different states of the state machine. The transitions between states are controlled by clicking in the respective buttons on the interface, represented here as connective arrows. The available buttons for each state are evidenced by the colors.

a) Disconnected State

The program is initialized in the *Disconnected* state. At this stage, the computer is not controlling the signal analyser, so, the only available actions are the ones that do not require any communication between both. The options available for the user at this point are: choosing the folder where the files will be saved; choosing and configuring the channels that will be recorded; connect the computer to the device. The channels configuration is exemplified in Figure 4.2 for the Channel 2. The channel boxes shown below can be seen in the full interface in Figure 4.3, on the left.

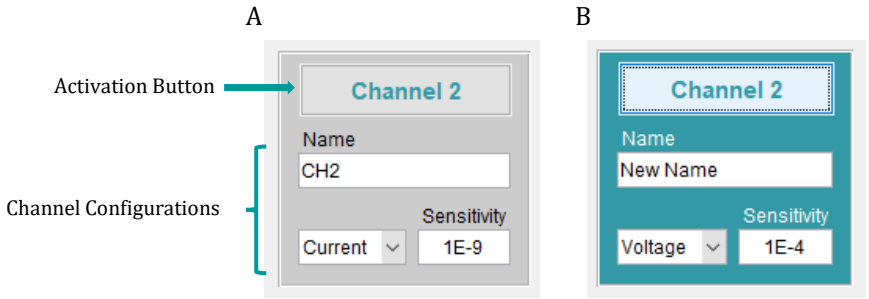

Figure 4.2. Channel Configuration: A) inactive Channel 2 with the default settings; B) activated and configured Channel 2.

Channels 2, 3 and 4 are inactive by default, since the experiments usually require one channel only (channel 1 by default). To activate other channels, the user must click on the button on the top of the associated channel box, as depicted in Figure 4.2. The green box indicates that the channel is active and will be recorded in the Recording state of the usage cycle. The name given to the channel will be used to later identify the file containing the data, as explained in the Recording state section. The user can also choose between "Current" and "Voltage" mode, and the sensitivity of the measurement. These two parameters are used to scale the signals sent by the signal analyser back to its original units (the signal collected was previously amplified which changed the units of the signals). We also introduce "Voltage" because it can be used a voltage amplifier instead of the current amplifier.

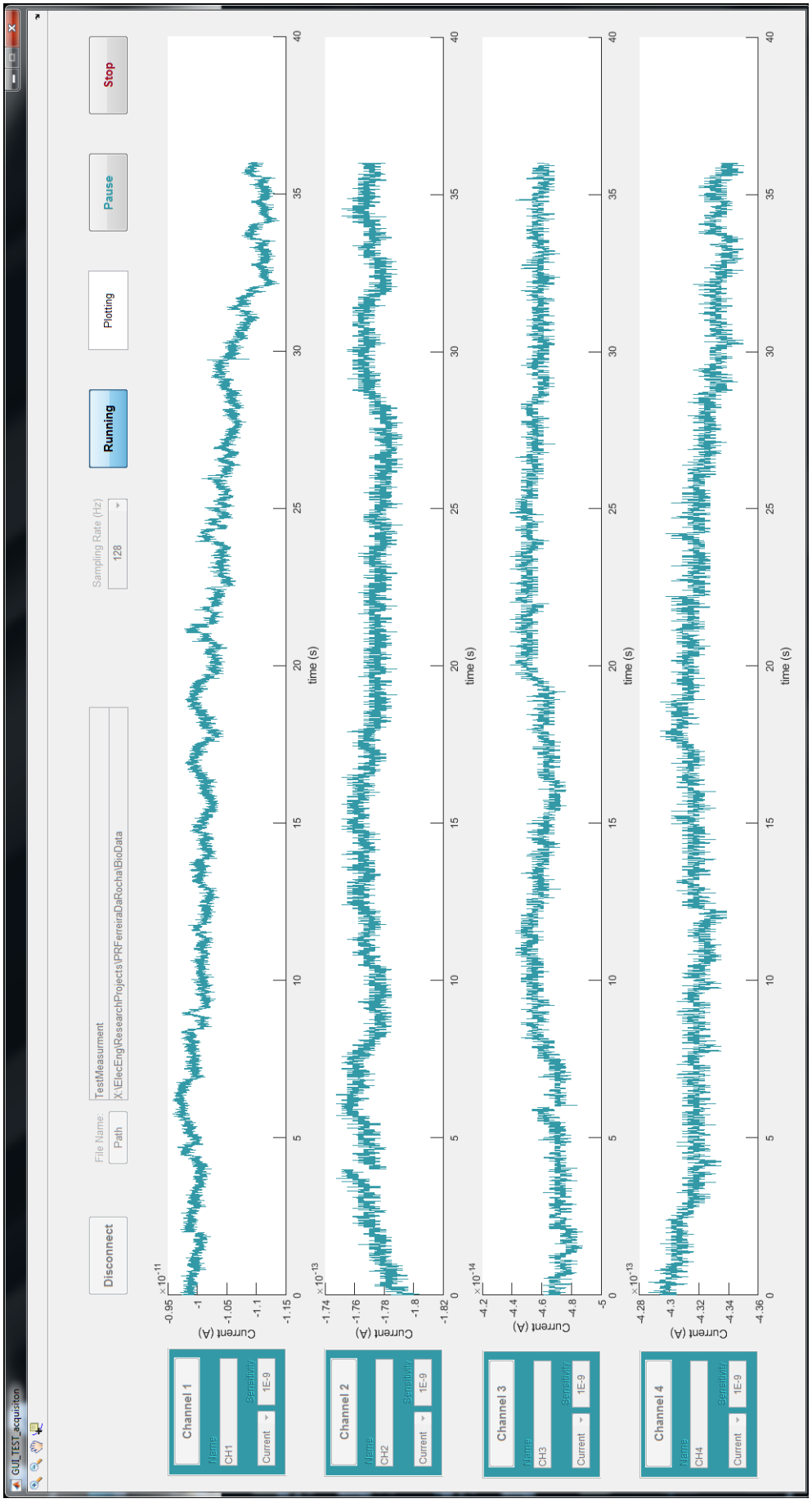

Figure 4.3. User interface of the Acquisition Software. The system is in the Recording state, where the only buttons unlocked are the "Pause" and "Stop" buttons. All the buttons related with the channels configuration and recording settings are locked. Each of the squares on the left is associated with a channel, being green when the channel is active and grey when it is inactive (in the figure shown they are all active).

b) Stopped State

As evidenced the diagram of Figure 4.1, when the user clicks on the "Connect" button, the state changes from *Disconnected* to *Stopped*. Now, the computer starts controlling the signal analyser. Commands can be sent from the computer to the instrument, such as the initial configurations for the recordings (which will not be detailed here). The appearance of the "Connect" button changes to "Disconnect", as it appears in Figure 4.3. All the configuring options available for the previous state (configuring the channels, path and filename) are still available on this state. However, now the sampling rate drop-down menu and the "Start" button are unlocked. The sampling rate options available are 64, 128 and 256 Hz. The signal analyser can work at higher sampling rates, but the acquisition rate is limited by the velocity of the Matlab program. The sampling rate of the Agilent 35670A is established by determining two parameters: the duration of the acquisition block and the number of acquired samples (limited to 256, 512, 1024 and 2048 points, in the time domain acquisition). Here, we fixed the number of points to the minimum available (256 points) because it is faster to plot. This way, when the user choses a certain sampling rate, it is actually establishing the time to acquire the 256 samples.

c) Recording State

To begin a recording, the user clicks in the button "Start", changing from *Stopped* to *Recording* state. The "Start" button changes to "Running" and is locked, as shown in Figure 4.3. All the elements of the interface become locked as well, except the "Stop" and "Pause" buttons. A folder is created in the path chosen. Its name is generated by combining the date, time and name set in the "File Name" text box (on the upper part of the inferface), in the form *Date_Time_FileName*. For example, in the case of Figure 4.3, the folder name would be:

2018.06.20_15h22_TestMeasurement

A text file is created for each active channel to save the data. The name of each file is created automatically based on the name in "File Name", the date, time and the channel name set by the user in the channel box (as shown in Figure 4.2), in the form *Data_Time_FileName_ChannelName*. For example, the name of the text file for channel 1 in Figure 4.3 would be:

2018.06.20_15h22_TestMeasurment_CH1.txt

Inside this folder is also saved a text file with the settings of the recording, such as the type of measurement (current or voltage) and the sensitivity of the recording for each channel. Then, the computer sends a command to the device to establish the sampling rate of the acquisition, and the recording cycle begins. In each iteration the computer commands the signal analyser to return the data blocks stored in the output buffer of the active channels. Then, the text file created for each channel is opened, and the data block is dropped there. The blocks are saved in the text file every iteration. The "data" variable of the acquisition loop of Matlab is then replaced every iteration with a new block. This avoids working with very long variables, which would occupy too much RAM and make the program run slower and slower as the recordings progress. The recently acquired signals are added to the plots, which are kept in *hold on* (Matlab terminology), enabling the user to see the full signal in real time.

The Matlab cycle and the acquisition cycle on the signal analyser need to be properly synchronized. As explained in section 4.1.3, the last block can be extracted from the buffer while a new block is being acquired. So, the Matlab reading cycle and the device acquisition cycle are synchronized as long as they have the same duration, because, this way, there will always be new data available in the

buffer. The duration of the device cycle is known – it was established when the user selected the sampling rate. So, to guarantee that the Matlab cycle has the same duration, each iteration is timed. After reading, saving and plotting the new data, the program enters in a countdown mode to guarantee that the full iteration as the same duration as the acquisition cycle of the signal analyser. The user can see the countdown in the status window of the interface (in Figure 4.3, the status window is in "Plotting" mode). As already mentioned the sampling rate is limited to 256 Hz. Higher sampling rates make the Matlab iterations take longer than the device acquisition cycle, leading to desynchrony between both.

This countdown mode is also useful to prevent the program from freezing. Every iteration a new data block is added to each of the active plots. This procedure starts getting slower with time (usually after several hours, depending on the processing capabilities of the computer) because Matlab is dealing with figures that have a high density of points. So, when the countdown mode detects that the cycle duration is close to the limit (that is, when the countdown begins very close to 0 s), the plots are cleared, making the program run faster again. This way it is guaranteed that the Matlab cycle has always the same duration. The user cannot see the first hours of recording, but they are still stored in the text files.

The only problem occurs when the device enters in auto-calibration mode. This is an automatic procedure of the signal analyser. The device stops acquiring data during the calibration, and the acquired signal will have a gap equivalent to one (or more) blocks. This situation cannot be avoided, but the gaps take only a few seconds in hours-long recordings, being neglectable.

d) Paused State

In the *Recording* state the user can click in "Pause" or "Stop". The "Pause" button will change the state to *Paused*, and "Stop" changes to *Stopped* state. In *Paused*, the Matlab cycle will wait for the user to either press this button again, which now appears as "Continue", or click in "Stop". These are the only options available. The *Paused* state is particularly convenient when the user needs to intervein in the sensor case for a short period of time but wishes to continue the recordings shortly after. The status window changes the message to "Paused" (in Figure 4.3 is currently showing "Plotting").

Clicking in "Continue" will resume the measurements by returning to *Recording* state. Clicking in "Stop" will change to *Stopped* state. The measurement is finish when the program reaches the *Stopped* state again. In this state the "Disconnect" button is unlocked. Changing to the state *Disconnected* makes the signal analyser independent of the computer again. This software architecture guaranteed a correct coordination between the controller and the device. The end user can acquire, save and monitor the activity of the cells in an easy and robust way.

4.2 Signal Analysis Software

The devices developed will be used to perform long-time measurements of cell populations. An efficient signal analysis tool is essential to examine such long recordings. The program developed provides an intuitive, immediate and insightful overview of dynamics of the bursting activity. It is presented with a simple and easy to use interface, developed in Matlab. In this sub-chapter, we will start by explaining the concept of the analysis software – section 4.2.1 – and show how the results provided can be easily examined and interpreted. Section 4.2.2 will be focused on the explanation of the algorithm implemented. Section 4.2.3 briefly describes the user-interface and how it is used.

4.2.1 The 3D Histograms: Concept and Analysis

The cooperative behaviour of the cell populations is evidenced by the electric spikes detected. Therefore, the spikes are the main element of interest when analysing the signals. The main parameters that characterize cell bursts are the spiking frequency, the amplitude and the width of the peaks. Figure 4.4 shows a very active bursting period of a glioma population, triggered by the addition of HCl to the cell medium, acquired with 1 mm^2 electrodes coated with PEDOT:PSS/CNT (the signal exemplified here will be presented later as well, in the measurements chapter, section 5.3, Figure 5.7).

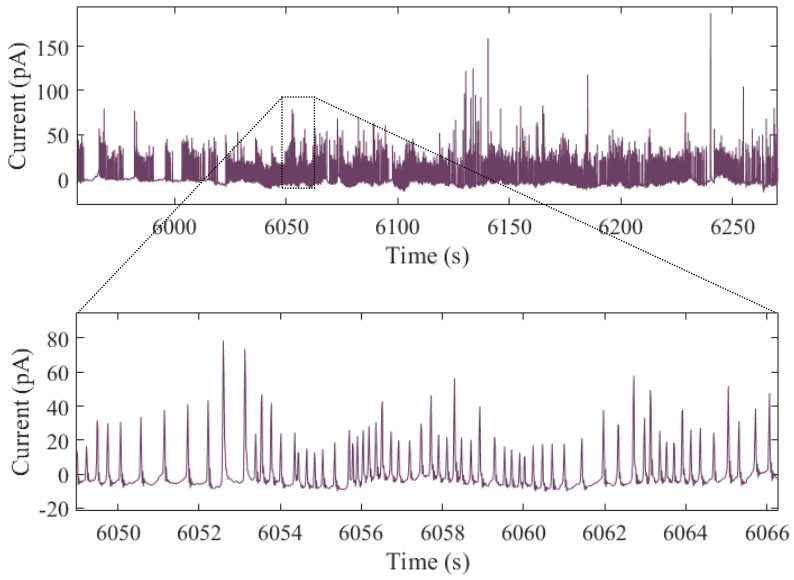

Figure 4.4. Very active bursting signal of a cell population, triggered by the addition of HCl. With the close-up shown in the bottom is possible to see the shape of the spikes.

With a close view it is possible to have an idea of the shape and frequency of the spikes in the zoomed-in region. A more effective way of doing this analysis is by calculating the histograms of the parameters of interest. Figure 4.5 shows the histograms of the Inter-Spike Interval (ISI), amplitude and width of the spikes detected in the signal of Figure 4.4. It is self-evident what the histograms of the amplitude and width of the spikes mean. The ISI histogram, however, is somewhat more indirect. The ISI is the time interval between two consecutive spikes. So, this histogram displays, in the X-axis bins, a

time scale associated with the interval between consecutive spikes and, in the Y-axis, the number of spikes that are separated by the each of these intervals. This particular type of histogram is a commonly used approach to characterize neuronal activity [107]–[113].

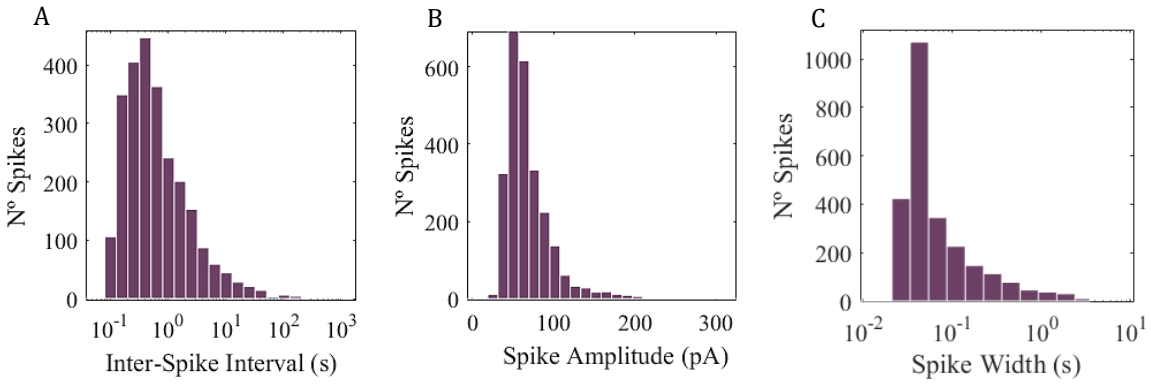

Figure 4.5. Histogram analysis of cell bursts: A) Inter-Spike Interval Histogram; B) Spike Amplitude Histogram; C) Spike Width Histogram.

By analysing the three histograms we can directly see that this bursting activity is mainly characterized by a spiking frequency that ranges mainly between 1 and 10 Hz (an ISI between 0.1 and 1 in Figure 4.5.A), an amplitude of 50 pA and a spike width of about 0.05 s. It is also possible to infer about the distribution of these parameters by evaluating the dispersion of the histogram peaks. For instance, the spike width is much more consistent than the ISI, meaning that even though the spikes may be separated by different periods of time, they tend to have approximately the same duration. It is also important to notice that the ISI and width histograms are more accurately represented by logarithmic bins.

Despite being a useful approach, this histogram analysis is still very limited because it does not provide any time information. This way it is not possible to evaluate how the signals evolve. Also, with the global histograms shown in Figure 4.5. the different parameters cannot be associated directly: the fact that, for instance, most spikes have a width of 0.05 s does not mean that these same spikes have an amplitude of 50 pA, because the maximum of each histogram could be associated with spikes that occurred at periods of the recording. So, time information is vital to have a clear overview of the dynamics of the bursting activity. This can be made by plotting a different histogram for each

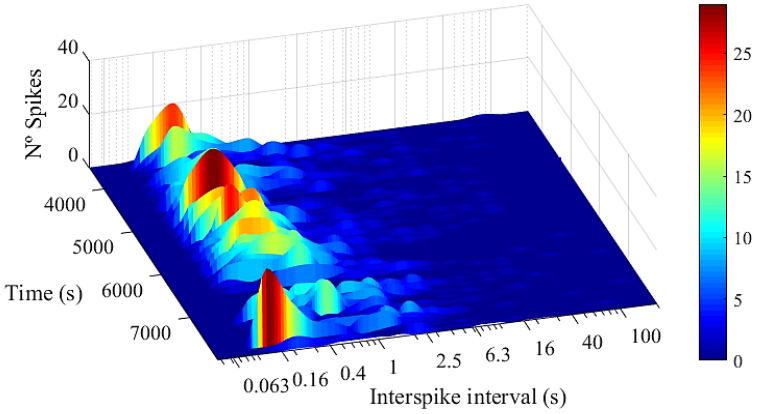

Figure 4.6. 3D histogram of the Inter-Spike Intervals. The resolution of the time axis is one histogram per 20 s. The resolution in the ISI axis is 5 bins per order of magnitude

portion of the signal (instead of a single histogram for the entire signal). Compiling all the histograms into a single plot generates a 3D graph where the third dimension added corresponds to the time axis, as shown in Figure 4.6. These type of 3D histograms are easier to analyse in a two-dimensional view, as represented in Figure 4.7 for all the three parameters.

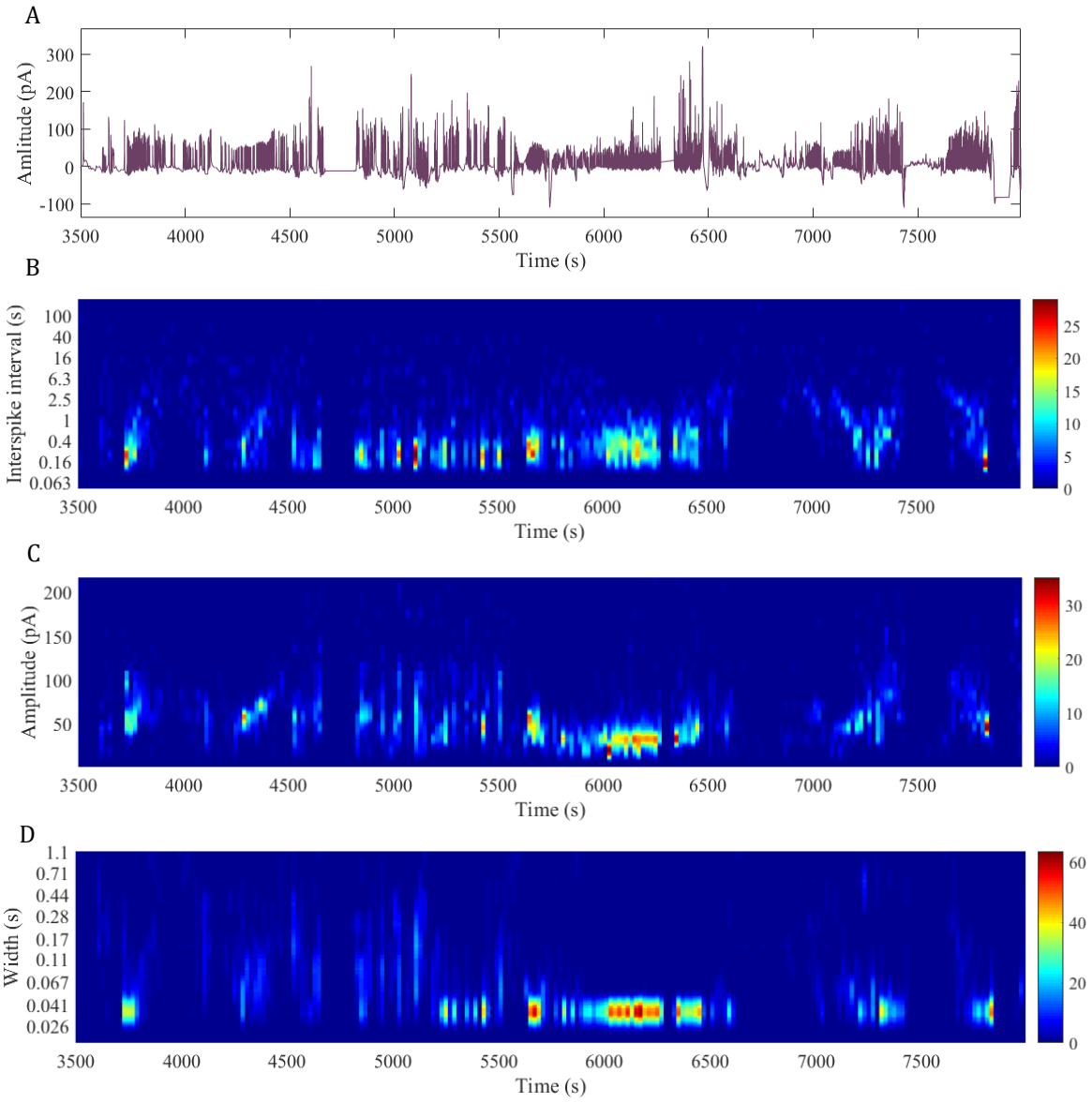

Figure 4.7. 3D histograms: A) recorded signal; B) 3D ISI histogram; C) 3D Amplitude histogram; D) 3D Width histogram. The time resolution of the 3D histograms is one histogram per 20 s.

This new way of representing the data is extremely informative. Together, the three graphs show how the number, shape and periodicity of the spikes change over time. The density of spikes can be evaluated in any of the three graphs, where redder regions correspond to higher spiking density. In the ISI plot, Figure 4.7.B, we can analyse the periodicity of the spiking activity. This graph shows that the population tends to fire every 0.16-0.4 seconds, when it is more active. We can conclude this because that is the interval where the maximums of the histograms are more concentrated. Also, very compact regions around a specific ISI mean that the periodicity is very consistent. So, besides seeing the prevalent spiking frequency, it is also possible to infer about how periodic the spikes are.

The 3D histogram of the amplitude and width show how the shape of the spikes changes with time (Figure 4.7.C and D). For example, until 5500 s, the spikes have very distinct shapes because there is a big dispersion of amplitudes and widths. However, from 5500 to 6500 s, the spikes acquire a consistent shape, with an amplitude of about 20 to 40 pA, and a width between 0.03 and 0.04 s. This can be verified in Figure 4.4.

This analysis tool is very powerful due to the vast and accessible information that it provides about the dynamics of the bursting behaviour. The activity is deconvoluted into its main properties, enabling a direct analysis of their changes with time.

4.2.2 3D Histogram Algorithm

This section will explain how the representations shown above were obtained. The algorithm can be divided in three main steps: a) baseline correction; b) peak detection; c) calculation of the 3D histograms. During this section we will use the signal shown previously, originated by the cell population after the addition of HCl and acquired with the PEDOT:PSS/CNT sensor with the 1 mm^2 electrodes.

a) Baseline Correction

The baseline of the signals collected in current mode varies considerably with time. Figure 4.8 shows the signal that was under analysis in the previous section before any pre-processing (the signal in Figure 4.4 had the baseline corrected). A baseline centred in 0 makes the peaks detection easier, being a very useful pre-processing step. The baseline is conventionally corrected using a digital high pass filter with a low frequency cut – the baseline is basically a low frequency background signal. However, this approach imposes a trade-off between the efficiency of the correction and the introduction of distortions to the signal of interest. We want to preserve the original shape of the spikes as much as possible, so a more complex an efficient method was developed.

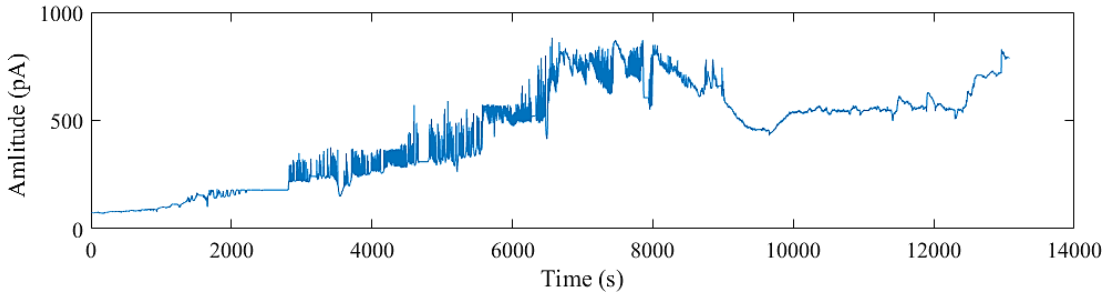

Figure 4.8. Raw signal of a cell population

It was done by first obtaining the baseline and then subtracting it to the signal. The calculation of the baseline is made in two steps: first, determine the averages of subsets of the signal; then interpolate all the local averages to create the baseline. The local averages are obtained with a moving window that calculates the mean for the portion of the signal under coverage. Instead of moving point-by-point, each new window is placed adjacently to the previous one. The size of the window determines the frequency cut-off of the baseline correction. If the window is too big, it may not be sensible to the higher frequency changes in the background signal that composes the baseline. On the other hand, if the size of the window is smaller than the width of a given spike, the window will go through the peak, calculate the averages along the curve, and obtain a baseline that attenuates (or eliminates) this spike. The window applied to this particular signal had a size correspondent to 5 s,

being small enough to fit the changes in the background baseline, but larger than the spikes under analysis (the spikes' width is evidenced in Figure 4.7.D).

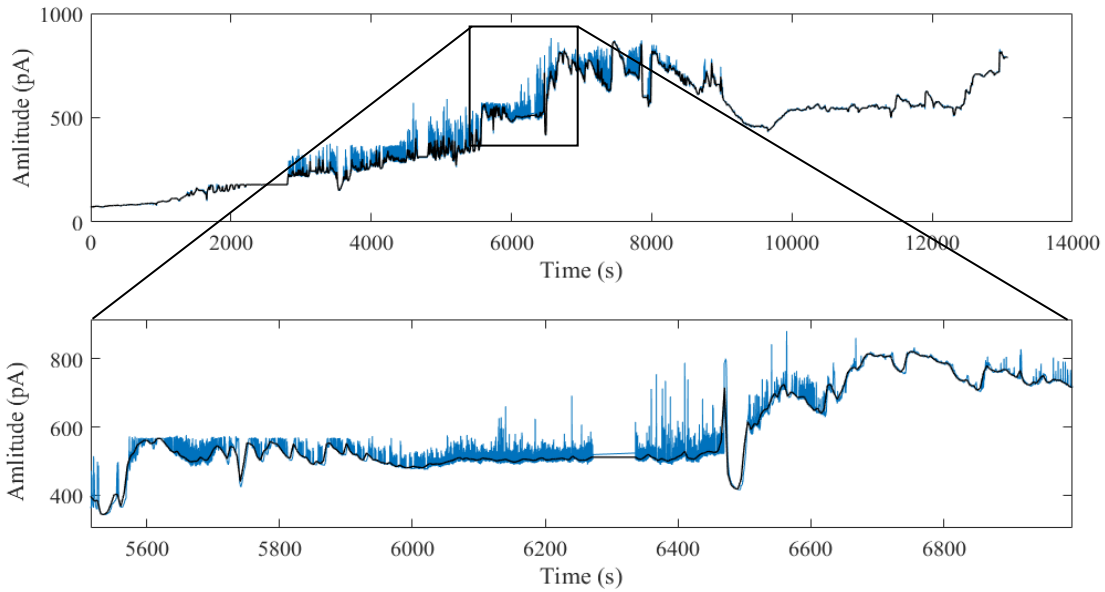

Figure 4.9. Baseline (in black) obtained for the signal. With the close-up shown in the bottom is possible to see how well the baseline is fitted to the raw signal.

As explained in section 4.2.3, this value can be changed in user-interface developed, to better fit the analysed signal. The average points obtained by the moving window are then connected with a linear interpolation creating the baseline depicted in Figure 4.9. It is also important to note that the data acquired did not require any denoising step. As seen in the Figure 4.4, the SNR is so high that the signal of interest is barely affected by the background noise. This guarantees that the shape of the spikes is preserved.

b) Spike Detection

After having a signal with a corrected baseline and centred in 0, the spikes can be found using the Matlab function *findpeaks*. This function accepts several inputs that are used to differentiate the peaks of interest from other local maximums. The parameters set for the spikes were: minimum peak height, minimum prominence, minimum and maximum peak width, and minimum peak distance. The meaning of the peak width and distance parameters are self-evident. The peak height and prominence are associated with the amplitude of the peak, but in different ways. The peak height is the Y coordinate of the maximum, that is, the spike amplitude counting from 0 (thus the importance of having a baseline centred in 0). The prominence, on the other hand, is related to how much a peak stands out from the inherent signal. It can be seen as the amplitude of the maximum counting from its own base (and from not 0). The prominence value translates the amplitude of the spike more accurately and, therefore, it was used to represent the amplitude histograms. The minimum prominence is a very useful parameter since it removes all the local maximums that may be associated with a high and noisy spike. We attributed the same threshold for the minimum height and prominence input of the function. The value of these parameters is determined automatically for any signal. This is done because the spikes of different signals may have very distinct amplitudes depending on the type of cells, sensors, sensor area, measuring mode (current or voltage), pH of the medium, etc. The method used to determine the height threshold for the spikes was based on the analysis of the signal's histogram. This histogram evidences the frequency of occurrence of the different amplitudes of the

signal. In Figure 4.10 is depicted the histogram of the signal under analysis, after the baseline correction. The histogram's curve will always have a peak centred in 0, associated with the baseline, as seen in Figure 4.10.A. The left and right limits (the least frequent amplitudes) will correspond to the positive and negative spikes. So, somewhere between the peak of the histogram and its upper/lower limits, there will be a point (associated with an amplitude) that can be used as a threshold for the spikes' height. This threshold is determined automatically for each histogram, according to the shape of its distribution. It was empirically verified that the point when the histogram's curve reaches 1 % of its maximum amplitude and slope establishes an efficient threshold for the spikes. These points are evidenced in Figure 4.10.A. In the example shown, the minimum heights obtained for the positive and negative spikes were, respectively, 10 and -21 pA. To detect the negative spikes, the signal is inverted and the *findpeaks* function is applied. The minimum height parameter in *findpeaks* is then the module of the negative threshold obtained (in signal of Figure 4.10.B, it would be 21 pA). In the case shown, we can see that some of the spikes detected do not correspond to real negative spikes. These can be removed by manually changing the parameters of the peak detection in the user-interface, as explained later in section 4.2.3.

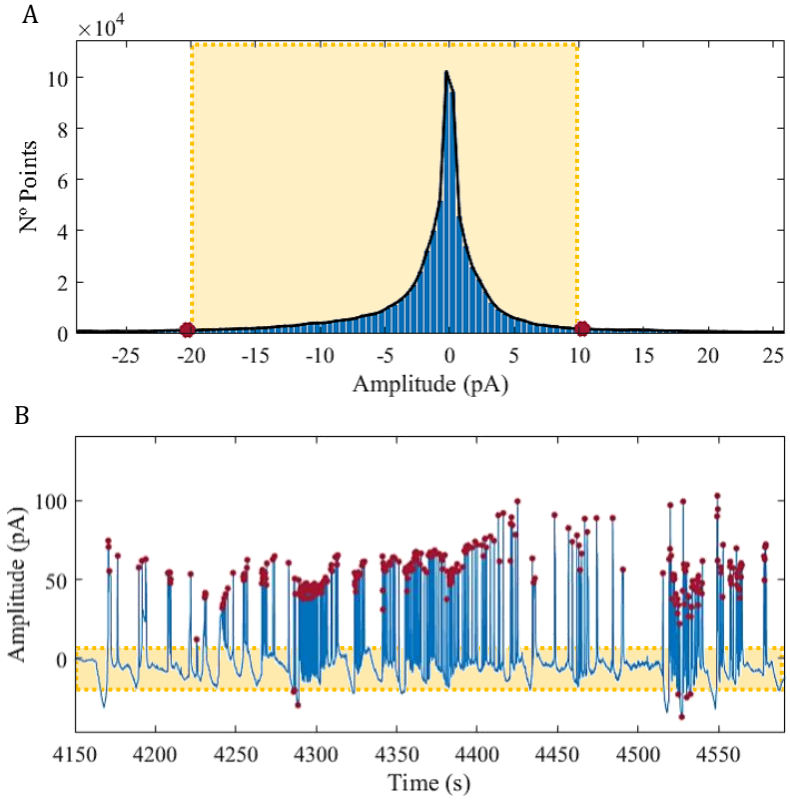

Figure 4.10. Height threshold for the spike detection: A) Histogram (blue) with the and threshold points obtained, in red; B) Signal and the spikes detected, in red. The yellow area (from -21 pA to 10 pA) represents the amplitude below the height threshold

The width of the peaks is calculated at the level correspondent to half of the prominence. The default values for the minimum width and peak distance were determined empirically and correspond to 2 sampling periods – their value varies with the sampling rate. It is considered that if a given portion of the signal is above the height threshold for at least two sampling periods than it must be a cell signal (which should be acquired at a higher sampling rate). The signal shown was acquired with a sampling rate of 64 Hz, therefore, the min width and the minimum peak distance is 0.0313 s. The default maximum width for the spikes is 3 s. Again, this default value was established considering

the acquired signals but can be changed in the user interface. The final result of the peak finding algorithm in shown in Figure 4.10.B, for a portion of the signal. The rate of success of the automatic peak detection is very high, having almost all the spikes detected. Changing the parameters manually after the automatic search increases this detection even further.

c) Calculation of the 3D Histogram

The final stage of the algorithm is calculating the 3D histograms presented before, in Figure 4.7. The function *findpeaks* returns vectors with the peak's prominence, width and position. The latter can be used to calculate a ISI vector, where each element corresponds the period between two consecutive peaks. The 3D histogram representations are obtained in several steps: 1) a moving window iteratively extracts the spikes detected; 2) the histograms of the different parameters are calculated for the spikes inside the window; 3) a curve is fitted to the histogram to create a smooth transition between the bars; 4) the different curves are compiled to create the 3D image. Figure 4.11.A evidences the spikes extracted from a given moving window and Figure 4.11.B shows the associated ISI histogram (similar histograms are calculated for the prominence and width of the spikes).

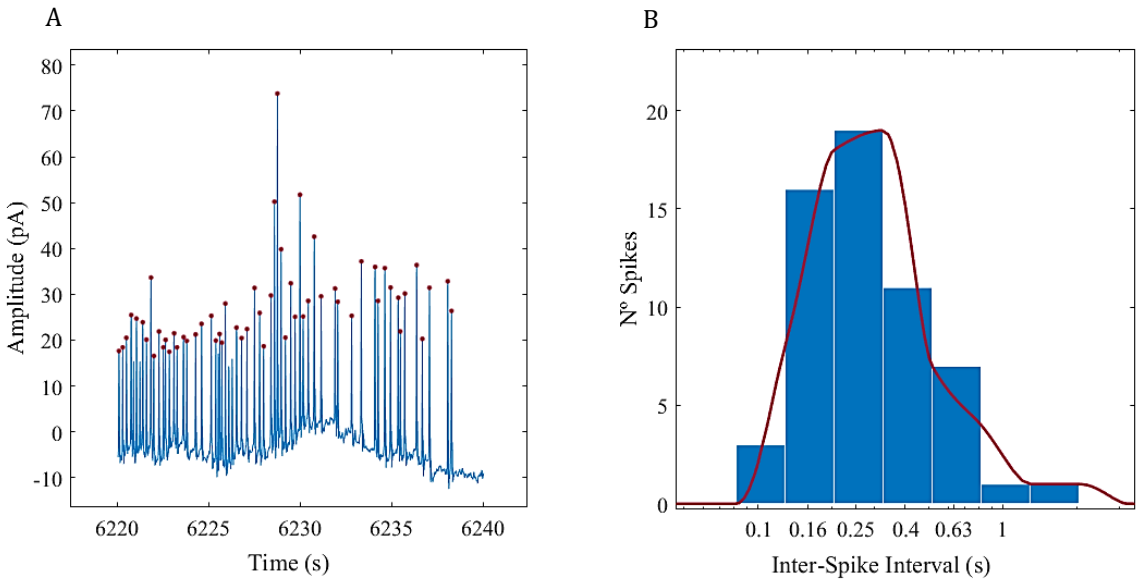

Figure 4.11. Example of the histogram calculated for each window: A) Spikes detected inside a moving window with a size of 20 s; B) ISI histogram of the spikes extracted and the correspondent fitting curve (in red).

Based on the analysis of many different signals, the default size of the moving window was set to 60 s. A smaller window increases the time resolution of the analysis, however, if it is too small, it cannot gather enough spikes and tends to generate histograms with small and isolated bars. In the signal exemplified here, we used a window of 20 s – the length of the signal portion shown Figure 4.11.A. The high spike density that resulted from the addiction of HCl enabled the window to be reduced and still encompass enough spikes to generate a proper histogram. This parameter can be adjusted in the user-interface as explained in the next section.

The bins of the histogram shown in Figure 4.11.B grow exponentially. The same applies for the width histogram. That is because the values of the ISI and width may vary in several orders of magnitude within the same signal. So, we are interested in having higher time resolution for the fast events, and lower resolution for the slower ones. This guarantees an adequate histogram shape as well. It was empirically established that five bins per order of magnitude enabled the data to be properly represented with a histogram. Figure 4.11.B evidences the centre of the bins in the X axis.

The amplitude histogram, in the other hand, could be represented with a linear bin size (instead of an exponentially increasing size), since the spike heights of a given measurement change within a smaller range. However, as already mentioned, the order of magnitude of the spikes recorded can vary significantly between measurements depending on the conditions of the recording. So, the size of these bins needs to be adjusted according to the amplitudes of the spikes of the signal under analysis. It was empirically verified that 25 bins equally distributed between the highest and lowest peak of the entire signal generates an adequate bar distribution of the resulting histogram.

A curve is fitted to each of the histograms obtained, as seen in Figure 4.11.B. This step will create a smoother 3D representation of the signal activity. The fitting must preserve the shape of the histogram as much as possible. The histogram profile rarely obeys any conventional distribution (such as normal or gamma distributions). So, the fitting was done with an interpolation between the bars. The interpolation used was the Piecewise Cubic Hermite Interpolating Polynomial (function *pchip* in Matlab) which proved to be flexible enough to fit to the shape of the different histograms and . The resulting fitted curve is represented in red in Figure 4.11.B.

4.2.3 User-Interface

It was developed a user-interface equipped with the algorithm described above. The main purpose of this program is enabling the user to easily analyse the files recorded with the acquisition software presented in section 4.1. The different default parameters that control the spike detection and histogram representation can be manipulated to guarantee the most suitable representation of the results.

The program is initialized with the window shown in Figure 4.12 (but with blank plots). Here, the user can click in the “Open” button (letter A in Figure 4.12) to search and load a signal, previously saved with the acquisition software. After loading the signal, it will appear in the upper plot. The baseline of the raw signal needs to be corrected. The default size of the moving window used in the baseline correction is 60 s. As already explained, this window needs to be small enough to properly fit to the changes of the baseline – which are in the minute range – but considerably larger than the spikes – which are in the second or sub-second range (depending on the signal). It was empirically verified that the value of 60 s stablished a suitable threshold between these two types of events, therefore being an efficient window size. Still, the size of the window can be changed through the edit text box evidenced with the letter B in Figure 4.12. In the example shown here, it was set to 20 s because the spikes of this particular signal are considerably faster than usual, as explained later in section 5.3. This allowed the size of the window to be reduced without compromising the shape of the spikes. Clicking in “Correct Baseline” (button C) will trigger the baseline correction algorithm. The baseline curve is added to the raw signal graph (in black) and the corrected signal is plotted in the lower graph. The user can inspect both signals using the zoom-in and zoom out-functions (tool bar represented with the letter E). The X and Y axis of the plots are linked so that a zoom applied in the upper graph is also applied in the lower one, and vice-versa. If the correction is not ideal, the moving window size can be changed, and the procedure repeated. By clicking the “save” buttons of the plots (shown with the F letter), the user can export the plots as images files or save them as Matlab figures.

Clicking in the button “Spike Analysis” (letter D in Figure 4.12) will trigger the spike detection algorithm. The window in Figure 4.13 is then presented to the user. The upper plot shows the spikes detected in orange, over the signal in green. The three 3D histograms are presented below the signal. The time axis of the four graphs is linked. This way, the user can zoom-in a given region of the any plot, and the have same region shown in the other three graphs.

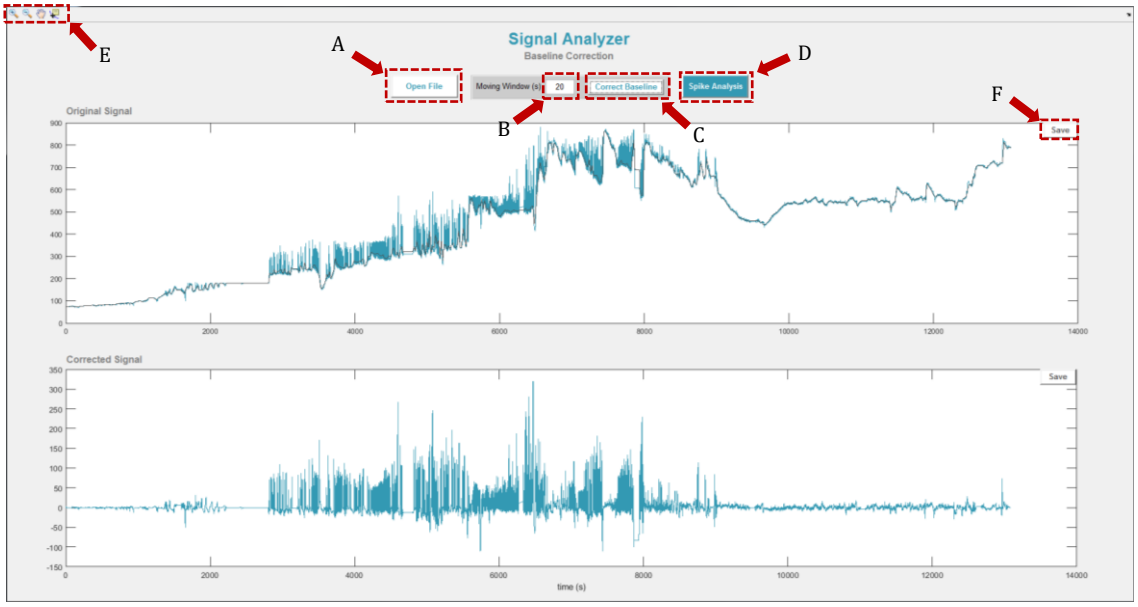

Figure 4.12. Initial window of the signal analysis software, where the user can load the files and correct the baseline: A) button to open file search; B) edit text box to change the default moving window size (60 s); C) button to execute the baseline correction; D) button to proceed to the spike detection and histogram analysis; E) tools to zoom-in, zoom-out, and inspect the plots; F) button to save the individual image.

The spike detection and histogram calculation are based on a set of default parameters. These include: the different thresholds set in the *findpeaks* function, the size of the time window used to calculate each histogram, and parameters to control the layout of the 3D histogram representations. The default values can be changed by the user in the settings menus. These are accessed by clicking in either “Spikes Settings” button (letter C in Figure 4.13) or “Histogram Settings” (letter D).

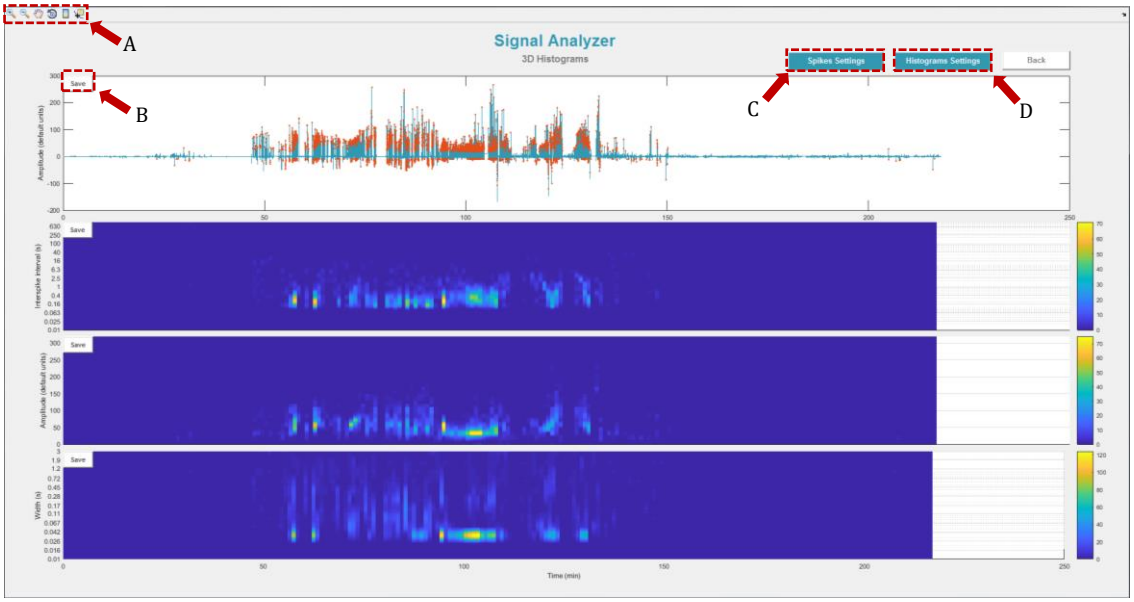

Figure 4.13. Spike analysis window, where the user can see the spikes detected (orange dots) and the resulting 3D histograms. The buttons evidenced enable the user to: A) zoom-in, zoom-out and inspect the plots; B) visualize and save the individual image; C) access the spikes settings menu to change the default parameters used for the spike detection; D) access the histogram settings menu to change the default parameters used for calculate and represent the 3D histograms.

4.3 Conclusion

In this chapter we presented the software developed to acquire and analyse the electrical signals. This is a major component of the overall system enabling the user study the activity of the cell population. Both platforms were developed in Matlab and integrated in user-friendly interfaces. With the acquisition program the user can control the measuring hardware (the dynamic signal analyser), control the recordings, view the monitoring results in real time, and store the measured data in the specified path. The analysis software is particularly useful to study the cooperative activity of the cells: it enables the end user to have a direct access to the fundamental parameters that characterize the bursting activity and how these change over time. These programs are already being used by the researchers at the University of Bath, UK.

The future work regarding the software is very vast because there is always margin to improve it by adding new features and functionalities to the programs. The main limitation of the acquisition software is the fact that it is device specific – it can only be used with the signal analyser 35670A from Agilent through a GPIB interface. Having the possibility of connecting the software to other devices would be very beneficial. The platform was completely developed from the ground up, so there are no drivers that can be simply downloaded and incorporated into the software. To use a different device, all the sets of configurations and commands would need to be already established in the software *a priori*, being ready to use according to the device selected. As for the analysis software, there are two major improvements to aim at. The first would be the addition of a statistical analysis applied to the parameters extracted (ex: how the average value and standard deviation of the parameters change with time). So far, the software extracts quantitative features of the spikes, but the actual analysis of these parameters can only be done qualitatively: it is based on the user evaluation of the 3D histograms generated. Statistical tools would provide useful results to compare different signals. A second improvement would be adding a functionality for spike classification and sorting. Given that the shape of the spikes can be traced back to their biological origins (in ways that are out of the scope of this thesis), sorting them would provide meaningful information about the different stages of cellular activity.

5 Cell Measurements

Epileptic seizures are a long-term debilitating disease remarkably frequent in glioma patients. With the use of LBE systems, a self-triggered cooperative electric activity in rat C6 glioma cell populations was already identified. This behaviour may be associated with the occurrence of seizures. However, there are still critical aspects that must be properly studied to verify the causality of these two events. A key milestone is proving that this event actually occurs in real human brain tumours. A very important intermediate step was performed in this dissertation: *in vitro* long-time recordings of glioma cells derived from a real patient, providing a much more reliable model of a real glioma. The measurements were made with the novel coated sensors, proving that they are suitable for monitoring cell populations. The signals collected were examined with the analysis software developed.

In this chapter we will explain the procedures applied to make the recordings and present the results obtained. In section 5.1 we describe the different elements of the ultra-sensitive experimental set-up. Section 5.2 is dedicated to the description of the cell culture. In section 5.3 we will present and analyse the results obtained in the recordings. We will then close this chapter by summarizing the main conclusions and presenting the future work related with the cell measurements.

5.1 Experimental Setup

The experimental setup needs to ensure two main requisites: low background noise and maintenance of the cell viability. This system is composed by: the sensor case, which has the sensor with the cultured cells; an incubator where the sensor case is inserted; a current amplifier connected to the sensor case; a dynamic signal analyser; and a computer with the acquisition software to control and monitor the recordings. This section will describe these components in further detail.

5.1.1 Sensor Case and Incubator

After sterilizing the sensor in ethanol for 2 h, the cell population was seeded inside the compartment shown in Figure 5.1.A. The cell culture covers the entire surface of the sensor inside the compartment. The sensor is inserted in a specific holder which is electrically coupled with the quadrangular gold connectors of the sensor. It also covers the compartment well with a lid to prevent medium evaporation. The sensor holder is inside a faraday cage, as shown in Figure 5.1.B. The wires seen in Figure 5.1.B are connected to the electrodes through the sensor holder.

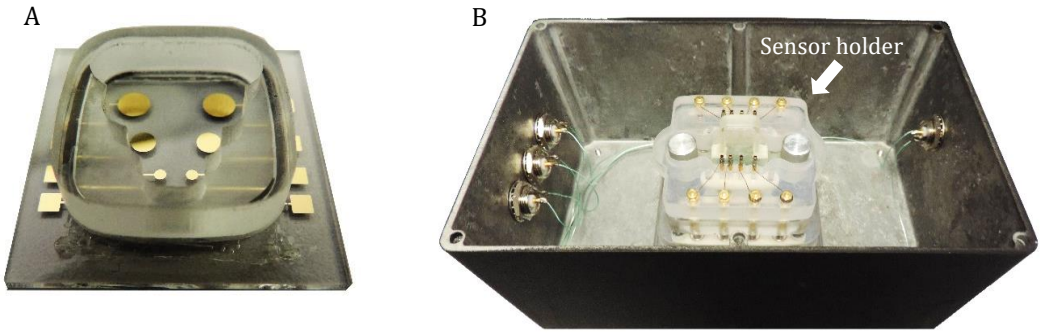

Figure 5.1. Sensor case for the cell measurements: A) sensor with the cell compartment; B) faraday cage with the sensor holder

The faraday cage is then sealed and put inside an incubator (Thermo Scientific Midi 40, Figure 5.2) that maintains the ideal biological conditions for the cell culture – 37 °C and 5 % CO_2. The wires of the sensor case are connected to the rest of the acquisition system through BNC ports installed on the wall of the incubator. All the connections are made with low-noise cables.

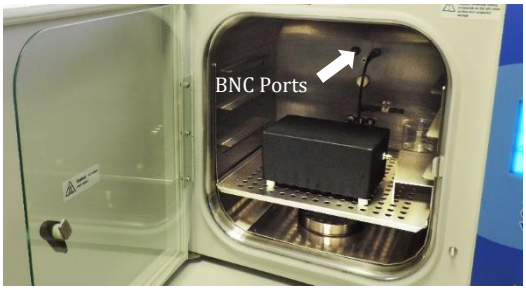

Figure 5.2. Incubator with the sensor case evidencing the BNC Ports installed on the incubator wall

This system ensures the viability of the cells for more than 24 h without medium change. The incubator can accommodate up to four sensor cases.

5.1.2 Pre-Amplifier

The signals generated by the cells need to be amplified before being digitalized. The current generated by glioma populations is in the pico-Ampere range, requiring a very sensible current amplifier. The low-noise current amplifier used – Stanford Research Systems SR570 (Figure 5.3) – is able to detect current fluctuations in the order of femto-Amperes, if properly configured. The pre-amplifier is kept inside a faraday cage to avoid electromagnetic interferences.

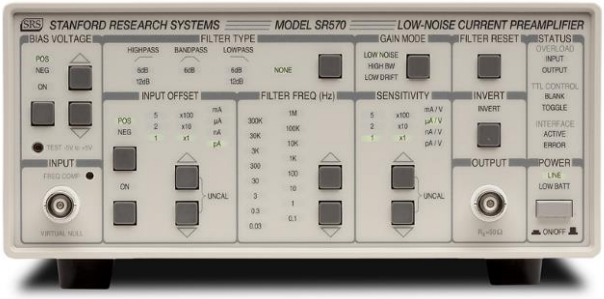

Figure 5.3. SR570 low-noise current preamplifier (image from www.thinksrs.com)

The current input is converted into a proportional voltage output with a sensitivity that can range from 1 mA/V to 1 pA/V. The sensitivity selected has a significant impact on the bandwidth and current noise of the amplifier, as evidenced in Figure 5.4. The plots shown correspond to the Low-Noise configuration of the amplifier. It is also possible to select a High Band-Width mode which enables the detection and amplification of higher frequency components. However, the current noise is higher in High Band-Width mode. Since the cells' signals are expected to have low frequency and amplitude it was chosen the Low-Noise Mode. The recordings were performed at a sensitivity of 1 nA/V, which generates a background noise in the femto Ampere range, Figure 5.4.A, and acts as a low-pass filter with a cut-off frequency of approximately 15 Hz, Figure 5.4.B.

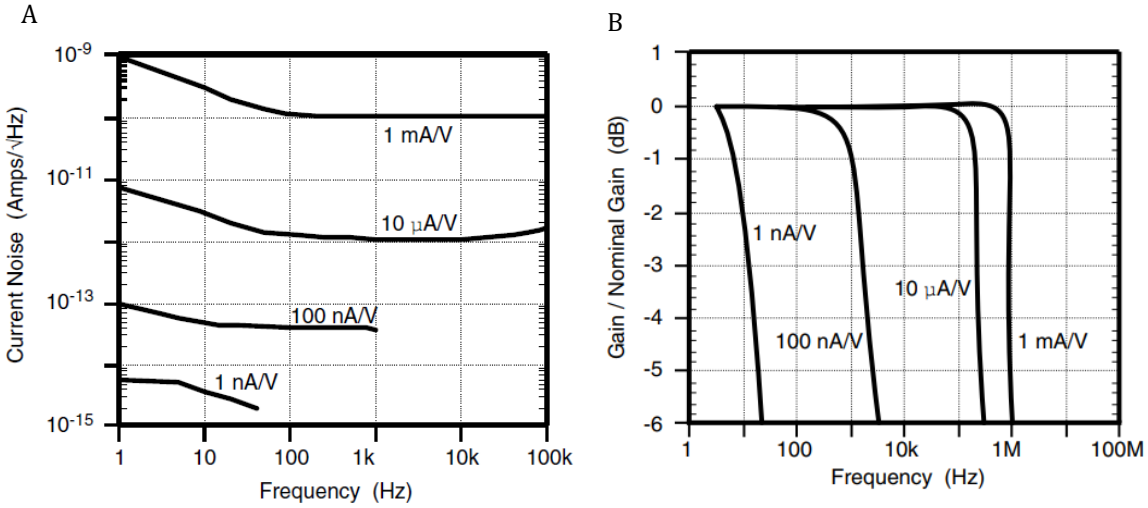

Figure 5.4. Influence of the sensitivity settings in the amplifier performance, in Low-Noise Mode: A) Current Noise vs. Frequency; B) Amplification Bandwidth (from SR570 datasheet)

The sensitivity may need to be adjusted to avoid signal overload. Choosing a very high sensitivity may lead to clipping in the output if the amplitude of the input signal increases significantly. The

lower sensitivity prevents clipping and expands the bandwidth allowing the detection of strong and high frequency signals. However, it also leads to a higher current noise.

5.1.3 Dynamic Signal Analyser

The voltage output of the current amplifier is sent to a Dynamic Signal Analyser 35670A from Agilent, a very high resolution AD convertor, shown in Figure 5.5. This Signal Analyser is capable of detecting very low voltage signals. It is also kept inside a faraday cage, next to the preamplifier.

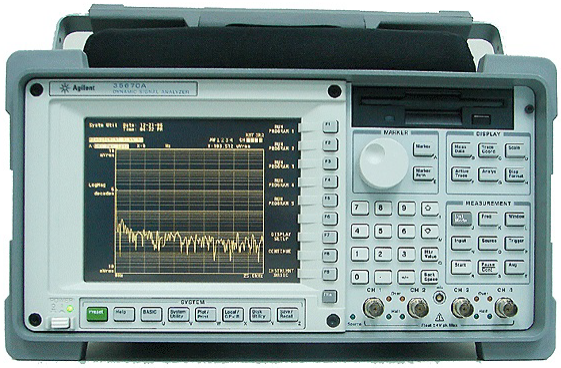

Figure 5.5. Dynamic Signal Analyser 35670A, Agilent (from www.keysight.com).

The measurements can be made in the time domain or frequency domain. As explained in section 4.1.1, the signal read is sent to the computer in data blocks (and not point-to-point), through a GPIB-USB-HS interface. The user can chose the sampling rate directly on the signal analyser by choosing the duration of the acquisition block and the number of acquired samples (the user-interface developed enables establishing the sampling rate in a more convenient way). As already mentioned in section 4.1.2, the device enables the recording of up to four channels simultaneously. The upper and lower limits of the sampling rate of the device are dependent on the number of channels used. For instance, when using only one channel, the sampling period can range from 3.815 μs to 2 s, while in four channels it ranges from 15.26 μsec to 8 sec. However, when coupled to the acquisition software, the actual limits of the sampling rate are constrained by the efficiency of the Matlab program – the acquisition period of the device cannot be faster than the acquisition period of the Matlab program.

The signal measured by the dynamic signal analyser is in voltage (output of the preamplifier) being proportional to the current signal generated by the cells. The acquisition software will then convert the signal back to its original units and display it on the screen of the computer.

5.2 Cell Culture

Rat C6 glioma cells are commonly used as a glioma model. This was also the case for the experiments performed with the gold LBEs (presented in section 2.3.2), where it was demonstrated that this population of cells can self-induce its bursting activity. However, the conclusions drawn can hardly be extrapolated to a real human glioma because the cells used are very different from those found in the human brain. So, it is important to reproduce these experiments with human glioma cells.

Glioblastoma is the most common and aggressive type of glioma [114]. Its expansion is driven by stem cell-like cells [115]. Here, we used Glioblastoma-derived Neural Stem (GNS) cell line to test the developed sensors and software. This cell line was derived from a real patient, so it consists in a good *in vitro* model of a human glioma. To the best of our knowledge, the cooperative electrical signalling of this cell line was never studied before. The results achieved here are significantly important, not only to evaluate the performance of the sensors, but also to study the activity of these cells and check if they also display the self-induced bursting activity.

The cell line was treated with Dulbecco's Modified Eagle Medium: Nutrient Mixture Ham's F-12 (DMEM/HAMS-F12) which is augmented with 15mM HEPES, sodium bicarbonate and L-glutamine (Sigma). To keep the cells undifferentiated, they were cultured in serum-free DMEM/HAMS-F12 media supplemented with N2 and B27 (Gibco), laminin (Cultrex) at 2 ug/ml, epidermal growth factor (EGF-mouse) and Fibroblast Growth Factor-2 (FGF-2) (Peprotech), 10ng/ml, as advised in [116], [117]. They were kept at 37°C with 5% CO_2 and the medium was changed every 3 days.

The plating on the sensors was done after cell dissociation with Accutase solution (Sigma) and centrifugation. The sensors and the cell compartment show in Figure 5.1.A were sterilized for 2 h in ethanol. A population of about 2000 GNS cells was cultured on the top of the sensors, inside the cell compartment, covering all the electrode pairs. The recordings were initiated 2 hours after the cell culturing, giving enough time for the cells to adhere to the sensor's surface.

5.3 Measurements Results

Rat C6 glioma cells exhibit self-induced bursting activity due to the passage of ions through ASICs at low pH. One of the objectives of this thesis was verifying if such behaviour also occurred in human glioma cells. The acquisition system presented above was used to perform long-time recordings of GNS populations. These measurements are also meant to demonstrate the suitability of the developed sensors in acquiring the cells signals. Given the characterization results presented in section 3.2, the sensor chosen for the recordings was the one coated with PEDOT:PSS/CNT. The PEDOT:PSS confers a low interfacial impedance, decreasing the thermal noise, and the CNT grants a high surface roughness, ideal for the cell anchoring, which decreases the signal attenuation of the extracellular recording.

Figure 5.6.A shows the first 18 hours of monitoring performed with the 2 mm² electrodes. During the initial 2 hours, the cells were displaying weak and uncorrelated electrical activity. This type of signalling is exemplified in Figure 5.6.B. It appears like a non-uniform noise, being the result of the weak random activity of the cells adhered to the electrodes. The actual background noise of the acquisition system cannot be accurately determined based on the signal of Figure 5.6.B because the noisy signal obtained is the combination of both the hardware noise and the random cell activity. However, since the resulting signal has an amplitude lower than 1 pA, the background noise of the acquisition system must be lower than this value (later we present a recording were the cells were silenced, and the only signal captured was the background noise of the acquisition system).

The bursting activity initiates two hours after the beginning of the recording. Such a delay was expected given the bursting mechanism proposed in section 2.2.3: the intense firing only occurs once the metabolism of the cancer cells lowers the pH of the medium. At this point, the population exhibits a synchronized electrical signalling, giving rise to the well-defined spikes shown in Figure 5.6.C.

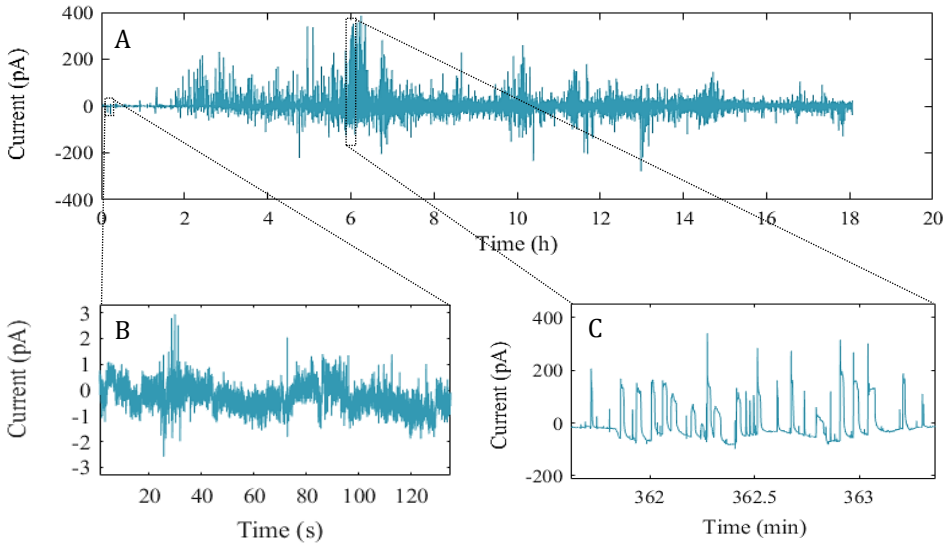

Figure 5.6. Cell measurements performed with the PEDOT:PSS/CNT coated sensor, with the 2 mm² electrodes: A) full 18 hours of recording; B) weak and random electrical activity; C) intense and synchronized electrical bursts.

As presented in section 2.3.2, the electrical spikes collected from C6 rat glioma cells with 10 mm² gold electrodes had a maximum amplitude of about 75 pA. The signals obtained here with the coated sensors had spikes with an amplitude of almost 400 pA (and were recorded with much

smaller electrodes which gathered a smaller population of adhered cells). This significant difference may be due to two different factors: either the human glioma cells display a much stronger electrical activity or the cell coupling to the developed sensors is significantly higher, leading to a lower signal attenuation and, therefore, a higher sensitivity.

The cell activity decays slowly with time. At the end of the first day, the population no longer displayed the strong electrical bursts recorded in the first hours. After two days the cells were silenced. At day 3, 20 µl of diluted HCl were added to the cell medium in order to retrigger the cell bursts. The signal obtained is shown in Figure 5.7.A (it was already presented and examined in section 4.2 as an example to explain the analysis software). The results corroborate the bursting mechanism proposed before: a pH triggered electrical activity.

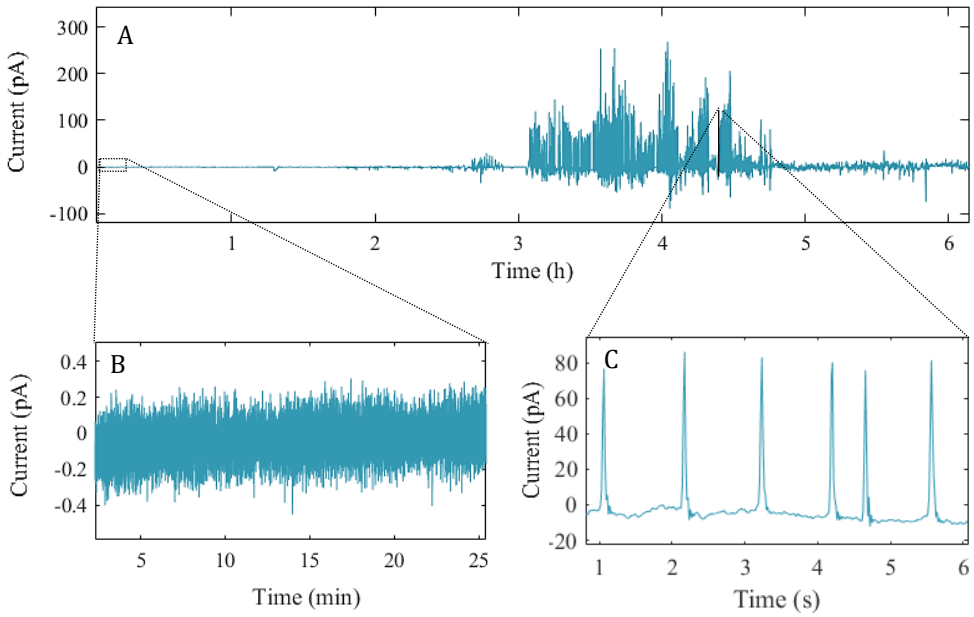

Figure 5.7. Cell measurements, performed with the sensor coated with PEDOT:PSS/CNT, with the 2 mm² electrodes after the addition of HCl to the cell medium: A) full 6 hours of recording; B) background noise of the measuring system; C) synchronized electrical bursts (the time label was readjusted for visualization purposes)

.

The HCl was added at time 0 (on the third day of recordings). For the first 2 hours, the cells were still silenced, revealing the actual background noise of the considered system. The noise has an amplitude of about 0.4 pA peak-to-peak, as evidenced in Figure 5.7.B. Such a low background noise is remarkably good – gold electrodes with an identical area were reported to have a background noise of 1 pA peak-to-peak [19]. The noise of the acquisition is neglectable compared to the amplitude of the spikes detected. It is important to mention again that no denoising step was applying to the signal.

The electrical bursts restart 3 hours after the addition of HCl. As seen in Figure 5.7.C, the amplitude of the spikes is lower than in day 1 and they are much faster and frequent (the X axis label was adjusted so that the time scale could be easily inspected). The developed software can now be used to perform a precise analysis of these different parameters. The 3D histograms obtained are presented in Figure 5.8. The histograms on the left correspond to the signal of Figure 5.6 and the ones on the right correspond to Figure 5.7. We will only compare the most active regions of both recordings.

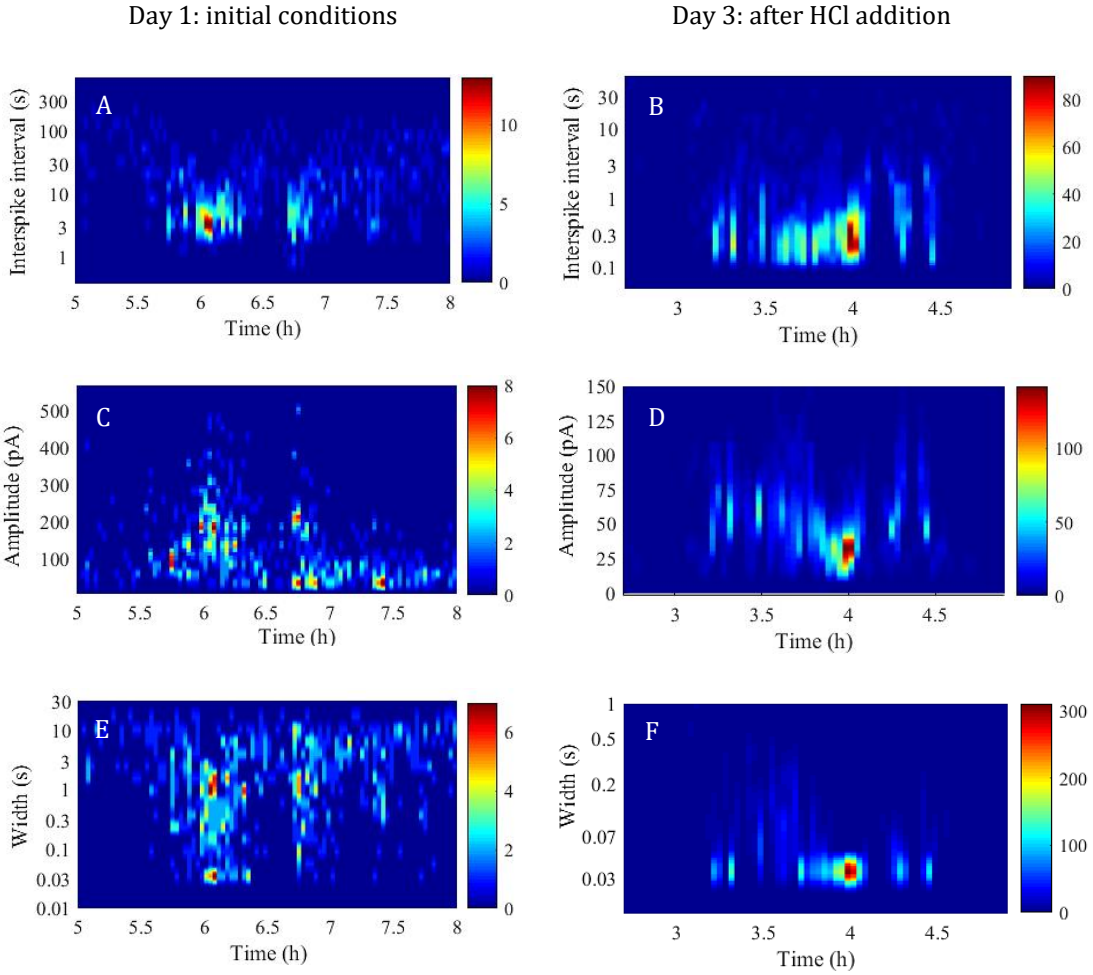

Figure 5.8. Comparison of the different spike parameters at day 1, under the initial conditions (left), and at day 3, after the addition of HCl to the cell medium (right): A) and B) 3D ISI histograms; C) and D) 3D amplitude histograms; E) and F) 3D width histograms. The resolution of the time axis is one histogram per 120 s. The histograms shown correspond to the most active regions of both recordings.

The spike density of the two bursting activities is significantly different. For every 120 s (time axis resolution of the 3D histograms), the cells in the acidified medium display a much higher number of spikes. This is evidenced by the scales with the number of spikes (colour maps in the side of each image). The interval between spikes, ISI, is then much lower for the cells under an acidified medium – the maximum and minimum values of ISI are one order of magnitude lower, as shown in Figures 5.8.A and B. On the first day, the intervals between the bursting spikes were between 3-10 s, while in the third day, after addiction of HCl, were between 0.3-1 s – 10 times faster. A correlation between the spiking frequency and periodicity can also be found in these two figures: as the spiking frequency increases (that is, as the values of ISI decrease) the spikes become more periodic (the ISI values are more compacted, having a defined peak). Both the amplitude and width of the spikes are higher during the measurements of day 1 (Figure 33.C and E). Taking a closer look at these two figures reveals that these two 3D histograms have inverse shapes. This exposes an interesting correlation between these parameters: as the amplitude of the spikes increases, their width decreases. Also, the spikes of day 1 have very inconstant shapes, evidenced by the dispersion of colours on the 3D histograms of the amplitude and width. In the most active regions, the amplitude ranges between 20 and 400 pA, and the width varies from 0.03 to 10 s. As already described in detail in section 4.2.1, after the addition of HCl, the spikes become highly periodic and with a consistent shape (low amplitude and fast).

5.4 Conclusion

This chapter presented the methods and results obtained in the cell measurements. It is the culmination of all the work achieved with this dissertation. All the technology developed was put to test in a real and state-of-the-art application: monitor and analyse the cooperative activity of human glioma populations. The experimental setup has ultra-low background noise and ensures the cell viability for more than 24 h. The fabricated devices were accoupled into this setup. The device chosen for the recordings was the LBE coated with PEDOT:PSS/CNT due to its low interfacial impedance and high potential for cell anchoring and adhesion. A population of GNS cells was cultured over the sensor. The background noise of the overall system has an amplitude of approximately 0.4 pA, significantly better than the state-of-the-art gold LBEs.

The results obtained show that, just like in the rat glioma cells, the human glioma populations too display a synchronized electrical activity. The intense electrical bursts is likely to be triggered at low pH. In a real brain glioma, this would occur naturally due to the cancer microenvironment. In this *in vitro* experiment, we waited for the metabolism of the cell culture to do the same. Later we enforced the bursting activity with the addition of a small quantity of HCl. The signals collected in both recordings are remarkable. The spikes reach an amplitude of hundreds of picoamperes, with a sub picoampere background noise. The sensors developed proved to be extremely efficient to monitor the cell populations.

The signal analysis software was then used to examine the bursting activity, revealing how the spiking dynamics change with time. The activity of the cells during the first day of recording was very different from that registered in the third day. After the addition of HCl, the signalling became much faster, uniform and periodic. The biological reasons for this change of behaviour are unknown (and out of the scope of this dissertation). It is possible that the bursts were originated by different mechanisms, such as different types of ion channels.

The future work regarding this topic should be focused in performing a deeper characterization of the measuring capabilities of the system considered (sensor and acquisition hardware). This characterization would start by a comparison of the background noise generated by the different coated electrodes – PEDOT:PSS, PEDOT:PSS/CNT and CNT – when connected to the rest of the instrumentation. While it is possible to accurately determine the background noise, the SNR, on the other hand, is not trivial to quantify and compare. It would be necessary to have the cells displaying a similar electric activity on each test and compare amplitudes of the signals collected by the different sensors. A more controlled way of making the glioma populations fire would be through electrical stimulation. Current pulses injected in the cell culture would induce electrical spikes. These would be recorded, and their amplitudes compared. According to the results obtained in the measurements, these experiments should be performed after the cells have displayed their self-induced electrical bursts, when it is guaranteed that only background noise is being captured (Figure 5.7.B). This way, the SNR can be accurately determined. The variable being studied with this experiment is the electrical coupling between the cells and the electrodes. It is expected that the rough CNT film would provide more anchoring points for the cells to adhere, reducing the cell cleft that separates them from the electrode surface, leading to a lower signal attenuation.

The biocompatibility would be evaluated with LIVE/DEAD imaging tests in order to compare the viability of cell populations adhered to the different sensors. The cell culture of each device would be submitted to periodical tests in the course of several days. After fully characterizing the measuring

capabilities of the different sensors, the most suitable one would be chosen to proceed with the neurological research of the glioma population. The developed sensors and software would be used to study the relation between glioma bursts and epileptic seizures. It is also important to note that this technology can be used to record and analyse the cooperative electric activity of other types of cells.

6 Conclusion

Gliomas frequently lead to epileptic seizures. The mechanisms behind this phenomenon have been widely studied but are not fully understood yet. This is in part due to the lack of tools available to monitor the ultra-weak electrical activity of glioma populations. MEAs, the standard technique used to measure the signals of neuron cultures, are not suitable for the task: the background noise generated by the micro-sized electrodes overshadows the weak glial signalling. Breakthrough sensors displaying a pair of large gold electrodes made the extracellular recording of glia/glioma populations possible for the first time. The aim of this project was to optimize this novel technology in order to use it in the prementioned neurological research. So, we developed new devices with enhanced sensing capabilities and an acquisition and analysis software designed to facilitate the study of the cellular signalling. This technology was then used to record and analyse, for the time, the synchronized electric activity of a human-derived glioma population.

6.1 Objectives and Achievements

The sensors were improved by coating its electrodes with porous films. We developed and compared three different devices, coated with either PEDOT:PSS, CNT, or both. The main objectives were to conceive a fabrication protocol, produce the three different sensors and characterize of the resulting devices, comparing them with the plain gold electrodes. The conceived fabrication procedure consisted in evaporating gold electrodes on glass substrates, followed by the drop-casting of 25 $\mu l/mm^2$ of each dispersion over the electrodes. The sensors were characterized in terms of their surface topography by AFM, and their interfacial impedance by EIS. The AFM images show that a CNT film confers a very high surface roughness, ideal to ensure cell adhesion. This improves the electrical coupling between cells and electrodes leading to a less attenuated signal and, consequently, a higher signal amplitude. The EIS results reveal that the three coated sensors have a much lower interfacial impedance than the gold electrodes, particularly at low frequencies. Below 10 Hz – the frequency range of glial signalling – the impedance is almost three orders of magnitude lower for the coated sensors. So, any of the three types of porous electrodes would be much more efficient in measuring glial/glioma activity. Despite having a smoother surface, PEDOT:PSS has the lowest interfacial impedance, meaning that it should generate the lowest thermal noise. So, to conclude, enhanced sensing devices were successfully developed with the fabrication protocol conceived. As confirmed by the characterization performed, both CNT and PEDOT:PSS confer beneficial properties to electrode surface, establishing these devices as promising biosensors to be used in the cell measurements.

Another major goal of this dissertation was to develop the software for signal acquisition and analysis so that the activity of the cell population could be easily recorded and studied. The acquisition software enables the user to command the dynamic signal analyser through the computer and extract the measured data. This way, with this interface, it is possible to control the recordings, visualize the signals in real time and store the data in the intended destination. The software developed to analyse the collected signals is particularly relevant for the end user of the devices. The goal was to conceive a method that enabled the user to examine the dynamics of the bursting activity in a simple and intuitive way. The routine implemented accomplished this by deconvoluting the bursting activity into its fundamental parameters – inter-spike interval, spike amplitude and width – and evidencing how these change overtime. The different parameters are represented in the form of 3D histograms where the X axis is time axis, the Y axis is the scale of the given parameter (ex: "Current (pA)" for the spike amplitude), and the Z axis shows how the spikes detected in a given time interval are distributed along the Y axis. By applying this paradigm to the three mentioned parameters, it is possible to immediately infer about the spike density, their shape and its consistency, the spiking frequency and its degree of periodicity. With this software, a large amount of information regarding the dynamics of the bursting activity is directly provided to the user. The information extracted could then be used to infer about the biological processes involved in the signalling, given the bursting dynamics exhibited.

The sensors and software developed were then used to record the electric activity of human-derived glioma populations. These measurements aimed at two goals: test and validate the tools developed, and verify whether the human glioma cells also displayed the synchronized activity found in rat cells. The recordings were made with the PEDOT:PSS/CNT sensor to take advantage of the properties of both materials. A culture of GNS cells derived from a real patient was deposited over the sensor which was later connected to the rest of acquisition system. The experimental setup had ultra-low background noise, granted by the very sensitive instrumentation shielded inside faraday cages, and connected with low-noise cables. The background noise of the overall system was 0.4 pA (registered once the cells were silenced). Such noise level is exceptionally good, imposing no limitation on the detection of the cells signalling. The electrical activity exhibited by the cells was remarkable as well: there were periods of uncorrelated activity – evidenced in the analysis software by a random distribution of values along the Y axis for inter-3D histogram – and periods of highly correlated bursting signalling – evidenced by the concentrated values in the 3D histograms. In these active regions, the analysis program enables the user to directly extract a lot of relevant information about the signalling dynamics. The spikes of the self-induced bursts registered in the first day occurred ay every 3 to 10 s, with amplitudes that ranged between 20 and 500 pA, and widths between 0.03 and 10 s. It was a low frequency signalling (between 0.1 and 0.3 Hz), with very dissimilar spikes. These reached significantly high amplitudes – much higher than those registered for rat glioma cells with the gold sensors. This can be due to the high sensitivity of the devices developed, to the remarkably intense activity of human glioma cells, or both. The HCl added on the third day made the silenced cells fire again, this time with very dense, periodic, fast and similar spikes, as evidenced by the uniform distributions on the 3D histograms. In the most active region the spikes occurred at intervals of 0.1 to 3 s – a spiking frequency considerably higher. So, important conclusions were drawn with these measurements: the sensor and acquisition hardware are very efficient for the cell recordings having neglectable background ground noise compared to the signals amplitude; the human glioma population too exhibit synchronized bursting activity; two very distinct types of bursting activity were iden-

tified which may be the result of different signalling mechanisms occurring in these cells. The objectives proposed were successfully achieved and the results obtained elevate the work developed to a state-of-the-art technology.

6.2 Future Work

It was demonstrated that both materials – CNT and PEDOT:PSS – conferred beneficial features to the sensors: the first is expected to grant a higher signal amplitude and the latter to lower the background noise of the recording. However, it is not clear which property has the most significant impact in the SNR. Future work should ascertain this with stimulation tests, by culturing a cell population over the different sensors, connecting them to the measuring instrumentation, and injecting current pulses on the culture. The current pulses would make the glioma cells fire in a more controlled and reproducible manner enabling a more accurate quantification of the SNR for the different devices. We also suggest performing LIVE/DEAD imaging tests on the cultures adhered to the electrodes. Several images should be taken in the course of several days to check which film ensures the highest cell viability. Once the best sensor is unambiguously selected, the fabrication protocol should be upgraded to a more reproducible procedure such as ink-jet printing. Using PCB or flexible polymeric subtracts instead of glass would also be beneficial for future applications. A PCB substrate would enable a significant design flexibility and the possibility of boosting the technology by employing circuitry in the device. Flexible polymeric substrates, on the other hand, enable the use of the device for *in vivo* applications.

The future work regarding acquisition software should be focused on making the platform compatible with other dynamic signal analysers, besides the 35670A from Agilent. As for the analysis software, we suggest the inclusion of a statistical analysis performed on the results of the 3D histogram to examine quantitatively the evolution of the different parameters. Spike classification and sorting algorithms would also be useful to identify the different types of bursting activity exhibited.

In a broader view, the technology developed, once optimized, should be used to proceed with the neurological research of the human glioma populations and their bursting activity. Controlled *in vitro* tests should be taken to determine which are the variables inducing and influencing the autonomous bursts, and what are the membrane mechanisms involved. As mentioned before, it was already reported that epileptic seizures can occur in mice brains, *in* vivo, due to the activation of glial ion channels in a low pH microenvironment. If these conclusions are proven to be applied for human gliomas, then future seizure therapies should seek to supress this autonomous electric activity of the tumour.

References

[1] R. D. Fields and B. Stevens-Graham, “Neuroscience: New insights into neuron-glia communication,” *Science,* vol. 298, no. 5593, pp. 556–562, 2002.

[2] M. L. Schroeter, O. Schmiedel, and D. Y. Von Cramon, “Spontaneous low-frequency oscillations decline in the aging brain,” *J. Cereb. Blood Flow Metab.*, vol. 24, no. 10, pp. 1183–1191, 2004.

[3] H. Obrig *et al.*, “Spontaneous low frequency oscillations of cerebral hemodynamics and metabolism in human adults,” *Neuroimage*, vol. 12, no. 6, pp. 623–639, 2000.

[4] M. L. Goodenberger and R. B. Jenkins, “Genetics of adult glioma,” *Cancer Genet.*, vol. 205, no. 12, pp. 613–621, 2012.

[5] A. Pitkänen and K. Lukasiuk, “Molecular and cellular basis of epileptogenesis in symptomatic epilepsy,” *Epilepsy Behav.*, vol. 14, no. 1 SUPPL. 1, pp. 16–25, 2009.

[6] R. S. Fisher *et al.*, “Epileptic seizures and epilepsy: Definitions proposed by the International League Against Epilepsy (ILAE) and the International Bureau for Epilepsy (IBE),” *Epilepsia*, vol. 46, no. 4, pp. 470–472, 2005.

[7] P. Jiruska *et al.*, “High-Frequency Network Activity, Global Increase in Neuronal Activity, and Synchrony Expansion Precede Epileptic Seizures In Vitro,” *J. Neurosci.*, vol. 30, no. 16, pp. 5690–5701, 2010.

[8] C. J. Vecht, M. Kerkhof, and A. Duran-Pena, “Seizure Prognosis in Brain Tumors: New Insights and Evidence-Based Management,” *Oncologist*, vol. 19, no. 7, pp. 751–759, 2014.

[9] T. S. Armstrong, R. Grant, M. R. Gilbert, J. W. Lee, and A. D. Norden, “Epilepsy in glioma patients: Mechanisms, management, and impact of anticonvulsant therapy,” *Neuro. Oncol.*, vol. 18, no. 6, pp. 779–789, 2016.

[10] M. De Groot, J. C. Reijneveld, E. Aronica, and J. J. Heimans, “Epilepsy in patients with a brain tumour: Focal epilepsy requires focused treatment,” *Brain*, vol. 135, no. 4, pp. 1002–1016, 2012.

[11] V. Franco, J. A. French, and E. Perucca, “Challenges in the clinical development of new antiepileptic drugs,” *Pharmacol. Res.*, vol. 103, pp. 95–104, 2016.

[12] M. Nowell, A. Miserocchi, and A. W. McEvoy, “Tumors in epilepsy,” *Semin. Neurol.*, vol. 35, no. 3, pp. 209–217, 2015.

[13] A. Beaumont and I. R. Whittle, “The Pathogenesis of Tumour Associated Epilepsy,” *Acta Neurochir. (Wien).*, vol. 142, no. 1, pp. 1–15, 2000.

[14] P. Marco, R. G. Sola, S. R. Y. Cajal, and J. DeFelipe, "Loss of inhibitory synapses on the soma and axon initial segment of pyramidal cells in human epileptic peritumoural neocortex: Implications for epilepsy," *Brain Res. Bull.*, vol. 44, no. 1, pp. 47–66, 1997.

[15] J. Pallud, L. Capelle, and G. Huberfeld, "Tumoral epileptogenicity: How does it happen'," *Epilepsia*, vol. 54, no. SUPPL. 9, pp. 30–34, 2013.

[16] J. Pallud *et al.*, "Cortical GABAergic excitation contributes to epileptic activities around human glioma," *Europe PMC Funders Group*, vol. 6, no. 244, pp. 1–27, 2015.

[17] A. Beaumont, M. Clarke, and I. R. Whittle, "The effects of malignant glioma on the EEG and seizure thresholds: An experimental study," *Acta Neurochir. (Wien).*, vol. 138, no. 4, pp. 370–381, 1996.

[18] M. C. R. Medeiros *et al.*, "An electrical method to measure low-frequency collective and synchronized cell activity using extracellular electrodes," *Sens. Bio-Sensing Res.*, vol. 10, pp. 1–8, 2016.

[19] P. R. F. Rocha *et al.*, "Electrochemical noise and impedance of Au electrode/electrolyte interfaces enabling extracellular detection of glioma cell populations," *Sci. Rep.*, vol. 6, no. April, pp. 1–10, 2016.

[20] P. R. F. Rocha *et al.*, "Extracellular electrical recording of pH-triggered bursts in C6 glioma cell populations," *Sci. Adv.*, vol. 2, no. 12, p. e1600516, 2016.

[21] A. L. G. Mestre *et al.*, "Extracellular Electrophysiological Measurements of Cooperative Signals in Astrocytes Populations," *Front. Neural Circuits*, vol. 11, no. October, pp. 1–9, 2017.

[22] X. Cui and D. C. Martin, "Electrochemical Deposition and Characterization of Poly (3,4-Ethylenedioxythiophene) on Neural Microelectrode Arrays," *Sens. Actuat B-Chem*, vol. 89, pp. 92–102, 2003.

[23] P. Leleux *et al.*, "Conducting Polymer Electrodes for Electroencephalography," *Adv. Healthc. Mater.*, vol. 3, no. 4, pp. 490–493, 2014.

[24] M. C. R. Medeiros *et al.*, "Performance assessment of polymer based electrodes for *in vitro* electrophysiological sensing: the role of the electrode impedance," in SPIE Organic Photonics + Electronics, vol. 9944, 2016.

[25] S. Garibaldi, C. Brunelli, and V. Bavastrello, "Carbon nanotube biocompatibility with cardiac muscle cells," *Nanotechnology*, vol. 17, pp. 391–397, 2006.

[26] T. Gabay, M. Ben-david, I. Kalifa, and R. Sorkin, "Electro-chemical and biological properties of carbon nanotube based multi-electrode," *Nanotechnology*, vol. 18, no. 3 , 2007.

[27] G. Cellot *et al.*, "Carbon nanotubes might improve neuronal performance by favouring electrical shortcuts," *Nature Technology,* vol. 4, pp. 126–133, 2008.

[28] A. Mazzatenta *et al.*, "Interfacing Neurons with Carbon Nanotubes : Electrical Signal Transfer and Synaptic Stimulation in Cultured Brain Circuits," *J. Neurosci.* vol. 27, no. 26, pp. 6931–6936, 2007.

[29] R. Gerwig *et al.*, "PEDOT–CNT Composite Microelectrodes for Recording and Electrostimulation Applications: Fabrication, Morphology, and Electrical Properties," *Front. Neuroeng.*, vol. 5, no. May, pp. 1–11, 2012.

[30] J. Bahney, S. Herculano-houzel, and C. Biology, “The Search for True Numbers of Neurons and Glial Cells in the Human Brain: A Review of 150 Years of Cell Counting,” *J Comp Neurol.,* vol. 524, no. 18, pp. 3865–3895, 2017.

[31] E. Wanke, F. Gullo, E. Dossi, G. Valenza, and A. Becchetti, “Neuron-glia cross talk revealed in reverberating networks by simultaneous extracellular recording of spikes and astrocytes’ glutamate transporter and K + currents,” *J. Neurophysiol.*, vol. 116, no. 6, pp. 2706–2719, 2016.

[32] S. Jäkel and L. Dimou, “Glial Cells and Their Function in the Adult Brain: A Journey through the History of Their Ablation,” *Front. Cell. Neurosci.*, vol. 11, no. February, pp. 1–17, 2017.

[33] A. J. Jiménez, M. D. Domínguez-Pinos, M. M. Guerra, P. Fernández-Llebrez, and J. M. Pérez-Fígares, “Structure and function of the ependymal barrier and diseases associated with ependyma disruption,” *Tissue Barriers*, vol. 2, no. 3, pp. 1–14, 2014.

[34] M. L. Olsen, B. S. Khakh, S. N. Skatchkov, M. Zhou, C. J. Lee, and N. Rouach, “New Insights on Astrocyte Ion Channels: Critical for Homeostasis and Neuron-Glia Signaling,” *J. Neurosci*., vol. 35, no. 41, pp. 13827–13835, 2015.

[35] J. A. Black et al., “Sodium channel mRNAs in cultured spinal cord astrocytes: in situ hybridization in identified cell types,” *Molecular Brain Research*, vol. 23, pp. 235–245, 1994.

[36] B. A. Barres, “Ion Channel Expression by White Matter Glia: The Type-l Astrocyte,” *Neuron*, vol. 5, pp. 527–544, 1990.

[37] B. A. Baetres, “Ion Channel Expression by White Matter Glia: I. Type 2 Astrocytes and Oligodendrocytes,” *Glia*, vol. 30, pp. 10–30, 1988.

[38] H. Sontheimer, “Voltage-dependent ion channels in glial cells,” *Glia*, vol. 11, no. 2, pp. 156–172, 1994.

[39] a Verkhratsky and H. Kettenmann, “Calcium signalling in glial cells.,” *Trends Neurosci.*, vol. 19, no. 8, pp. 346–52, 1996.

[40] A. Verkhratsky and C. Steinhauser, “Ion channels in glial cells,” *Brain Research Reviews*, pp. 380–412, 2000.

[41] C. Huang et al., “Existence and distinction of acid-evoked currents in rat astrocytes,” *Glia*, vol. 58, no. 12, pp. 1415–1424, 2010.

[42] Y. C. Lin, Y. C. Liu, Y. Y. Huang, and C. C. Lien, “High-density expression of Ca2+-permeable ASIC1a channels in NG2 glia of rat hippocampus,” *PLoS One*, vol. 5, no. 9, pp. 1–8, 2010.

[43] D. H. Feldman et al., “Characterization of acid-sensing ion channel expression in oligodendrocyte-lineage cells,” *Glia*, vol. 56, no. 11, pp. 1238–1249, 2008.

[44] C. Neusch, “Lack of the Kir4.1 Channel Subunit Abolishes K+ Buffering Properties of Astrocytes in the Ventral Respiratory Group: Impact on Extracellular K+ Regulation*,” J. Neurophysiol.*, vol. 95, no. 3, pp. 1843–1852, 2006.

[45] V. Parpura, T. A. Basarsky, F. Liu, K. Jeftinija, S. Jeftinija, and P. G. Haydon, “Glutamate-mediated astrocyte-neuron signalling,” *Nature*, vol. 369, no. 6483, pp. 744–747, 1994.

[46] S. Kirischuk, H. Kettenmann, and A. Verkhratsky, “Na+/Ca2+ exchanger modulates kainate-triggered Ca2+ signaling in Bergmann glial cells in situ.,” *FASEB J.*, vol. 11, no. 7, pp. 566–72, 1997.

[47] T. Brismar, “Physiology of transformed glial cells,” *Glia*, vol. 15, no. 3, pp. 231–243, 1995.

[48] B. K. Berdiev et al., “Acid-sensing ion channels in malignant gliomas,” *J. Biol. Chem*., vol. 278, no. 17, pp. 15023–15034, 2003.

[49] N. Kapoor et al., “Knockdown of ASIC1 and epithelial sodium channel subunits inhibits glioblastoma whole cell current and cell migration,” *J. Biol. Chem*., vol. 284, no. 36, pp. 24526–24541, 2009.

[50] C. Labrakakis, S. Patt, J. Hartmann, and H. Kettenmann, “Glutamate receptor activation can trigger electrical activity in human glioma cells,” *Neuroscience*, vol. 10, no. February, pp. 2153–2162, 1998.

[51] M. E. Spira and A. Hai, “Multi-electrode array technologies for neuroscience and cardiology,” *Nat. Nanotechnol*., vol. 8, no. 2, pp. 83–94, 2013.

[52] L. Berdondini, K. Imfeld, A. Maccione, M. Tedesco, and S. Neukom, “Active pixel sensor array for high spatio-temporal resolution electrophysiological recordings from single cell to large scale neuronal networks,” *Lab on a Chip*, vol. 9, no. 18, 2009.

[53] D. Eytan and S. Marom, “Dynamics and Effective Topology Underlying Synchronization in Networks of Cortical Neurons,” *J. Neurosci*., vol. 26, no. 33, pp. 8465–8476, 2006.

[54] M. Hutzler et al., “High-Resolution Multitransistor Array Recording of Electrical Field Potentials in Cultured Brain Slices,” *J. Neurophysiol.*, pp. 1638–1645, 2018.

[55] U. Frey, U. Egert, F. Heer, S. Hafizovic, and A. Hierlemann, “Microelectronic system for high-resolution mapping of extracellular electric fields applied to brain slices,” *Biosens. Bioelectron.*, vol. 24, pp. 2191–2198, 2009.

[56] D. Braun and P. Fromherz, “Fluorescence interference-contrast microscopy of cell adhesion on oxidized silicon,” *Appl. Phys. A Mater. Sci. Process.*, vol. 65, no. 4–5, pp. 341–348, 1997.

[57] Y. Iwanaga, D. Braun, and P. Fromherz, “No correlation of focal contacts and close adhesion by comparing GFP-vinculin and fluorescence interference of DiI,” *Eur. Biophys. J*., vol. 30, no. 1, pp. 17–26, 2001.

[58] R. Gleixner and P. Fromherz, “The extracellular electrical resistivity in cell adhesion,” *Biophys. J.*, vol. 90, no. 7, pp. 2600–2611, 2006.

[59] A. L. G. Mestre et al., “Ultrasensitive gold micro-structured electrodes enabling the detection of extra-cellular long-lasting potentials in astrocytes populations,” *Sci. Rep*., vol. 7, no. 1, pp. 1–11, 2017.

[60] C. Xie, Z. Lin, L. Hanson, Y. Cui, and B. Cui, “Intracellular recording of action potentials by nanopillar electroporation,” *Nat. Nanotechnol*., vol. 7, no. 3, pp. 185–190, 2012.

[61] W. Dabrowski, P. Grybos, and A. M. Litke, “A low noise multichannel integrated circuit for recording neuronal signals using microelectrode arrays,” *Biosens. Bioelectron.*, vol. 19, pp. 749–761, 2004.

[62] M. E. J. Obien, K. Deligkaris, T. Bullmann, D. J. Bakkum, and U. Frey, “Revealing neuronal function through microelectrode array recordings,” *Front. Neurosci*., vol. 9, no. JAN, p. 423, 2015.

[63] A. Blau, “Cell adhesion promotion strategies for signal transduction enhancement in microelectrode array in vitro electrophysiology: An introductory overview and critical discussion,” *Curr. Opin. Colloid Interface Sci*., vol. 18, no. 5, pp. 481–492, 2013.

[64] A. Hai et al., “Spine-shaped gold protrusions improve the adherence and electrical coupling of neurons with the surface of micro-electronic devices,” *J. R. Soc. Interface*, vol. 6, no. 41, pp. 1153–1165, 2009.

[65] N. Shmoel, N. Rabieh, S. M. Ojovan, H. Erez, E. Maydan, and M. E. Spira, “Multisite electrophysiological recordings by self-assembled loose-patch-like junctions between cultured hippocampal neurons and mushroom-shaped microelectrodes,” *Sci. Rep*., vol. 6, no. January, pp. 1–11, 2016.

[66] C. Xie, L. Hanson, W. Xie, Z. Lin, B. Cui, and Y. Cui, “Noninvasive neuron pinning with nanopillar arrays,” *Nano Lett.*, vol. 10, no. 10, pp. 4020–4024, 2010.

[67] W. Franks, I. Schenker, P. Schmutz, and A. Hierlemann, “Impedance characterization and modeling of electrodes for biomedical applications,” *IEEE Trans. Biomed. Eng*., vol. 52, no. 7, pp. 1295–1302, 2005.

[68] E. T. Mcadams, a Lackermeier, J. a Mclaughlin, D. Macken, and J. Jossinet, “The Linear and Nonlinear Electrical-Properties of the Electrode-Electrolyte Interface,” *Biosens. Bioelectron.,* vol. 10, pp. 67–74, 1995.

[69] M. H. Martin and A. Lasia, “Influence of experimental factors on the constant phase element behavior of Pt electrodes,” *Electrochim. Acta*, vol. 56, no. 23, pp. 8058–8068, 2011.

[70] S.-L. Wu, M. E. Orazem, B. Tribollet, and V. Vivier, “Impedance of a Disk Electrode with Reactions Involving an Adsorbed Intermediate: Experimental and Simulation Analysis,” *J. Electrochem. Soc*., vol. 156, no. 7, p. C214, 2009.

[71] J. B. Jorcin, M. E. Orazem, N. Pébère, and B. Tribollet, “CPE analysis by local electrochemical impedance spectroscopy,” *Electrochim. Acta*, vol. 51, no. 8–9, pp. 1473–1479, 2006.

[72] Z. Kerner and T. Pajkossy, “Impedance of rough capacitive electrodes: The role of surface disorder,” *J. Electroanal. Chem*., vol. 448, no. 1, pp. 139–142, 1998.

[73] J. Valsa, P. Dvořák, and M. Friedl, “Network model of the CPE,” *Radioengineering*, vol. 20, no. 3, pp. 619–626, 2011.

[74] B. A. Hierlemann, U. Frey, S. Hafizovic, and F. Heer, “Growing Cells Atop Microelectronic Chips,” *Proc. IEEE,* vol. 99, no. 2, 2011.

[75] B. Grobben, P. P. De Deyn, and H. Slegers, “Rat C6 glioma as experimental model system for the study of glioblastoma growth and invasion,” *Cell Tissue Res*., vol. 310, no. 3, pp. 257–270, 2002.

[76] P. Swietach, A. Hulikova, R. D. Vaughan-Jones, and A. L. Harris, “New insights into the physiological role of carbonic anhydrase IX in tumour pH regulation,” *Oncogene*, vol. 29, no. 50, pp. 6509–6521, 2010.

[77] F. Yang et al., “Astrocytic Acid-Sensing Ion Channel 1a Contributes to the Development of Chronic Epileptogenesis,” *Sci. Rep*., vol. 6, no. August, pp. 1–14, 2016.

[78] Y. Wen and J. Xu, “Scientific Importance of Water-Processable PEDOT–PSS and Preparation, Challenge and New Application in Sensors of Its Film Electrode: A Review,” *J. Polym. Sci. Part A Polym. Chem.*, vol. 55, no. 7, pp. 1121–1150, 2017.

[79] A. Schander, T. Teßmann, S. Strokov, H. Stemmann, A. K. Kreiter, and W. Lang, "In-vitro Evaluation of the Long-term Stability of PEDOT: PSS Coated Microelectrodes for Chronic Recording and Electrical Stimulation of Neurons," in 38th Annual International Conference of the IEEE Engineering in Medicine and Biology Society, pp. 6174–6177, 2016.

[80] M. Bongo et al., "PEDOT:gelatin composites mediate brain endothelial cell adhesion," *J. Mater. Chem. B*, vol. 1, no. 31, p. 3860, 2013.

[81] H. Park, S. Ko, J. Park, J. Y. Kim, and H. Song, "Redox-active charge carriers of conducting polymers as a tuner of conductivity and its potential window," *Sci. Rep.,* pp. 1–6, 2013.

[82] J. Rivnay et al., "High-performance transistors for bioelectronics through tuning of channel thickness," *Sci. Adv*., vol. 1, no. 4, pp. e1400251–e1400251, 2015.

[83] S. Löffler, B. Libberton, and A. Richter-Dahlfors, "Organic Bioelectronic Tools for Biomedical Applications," *Electronics*, vol. 4, no. 4, pp. 879–908, 2015.

[84] A. G. MacDiarmid et al., "The Concept of `Doping' of Conducting Polymers: The Role of Reduction Potentials [and Discussion]," *Philos. Trans. R. Soc. A Math. Phys. Eng. Sci*., vol. 314, no. 1528, pp. 3–15, 1985.

[85] E. Stavrinidou et al., "Direct measurement of ion mobility in a conducting polymer," *Adv. Mater*., vol. 25, no. 32, pp. 4488–4493, 2013.

[86] X. T. Cui and D. D. Zhou, "Poly (3,4-ethylenedioxythiophene) for chronic neural stimulation," *IEEE Trans. Neural Syst. Rehabil. Eng*., vol. 15, no. 1, pp. 502–508, 2007.

[87] S. J. Wilks, S. M. Richardson-burns, J. L. Hendricks, D. C. Martin, and K. J. Otto, "Poly (3 , 4-ethylenedioxythiophene) as a micro-neural interface material for electrostimulation," *Front. Neuroeng*., vol. 2, no. June, pp. 1–8, 2009.

[88] S. M. Richardson-Burns, J. L. Hendricks, B. Foster, L. K. Povlich, D. H. Kim, and D. C. Martin, "Polymerization of the conducting polymer poly(3,4-ethylenedioxythiophene) (PEDOT) around living neural cells," *Biomaterials*, vol. 28, no. 8, pp. 1539–1552, 2007.

[89] B. Wei, J. Liu, L. Ouyang, C. C. Kuo, and D. C. Martin, "Significant Enhancement of PEDOT Thin Film Adhesion to Inorganic Solid Substrates with EDOT-Acid," *ACS Appl. Mater. Interfaces*, vol. 7, no. 28, pp. 15388–15394, 2015.

[90] I. Cruz-Cruz, M. Reyes-Reyes, M. A. Aguilar-Frutis, A. G. Rodriguez, and R. López-Sandoval, "Study of the effect of DMSO concentration on the thickness of the PSS insulating barrier in PEDOT:PSS thin films," *Synth. Met*., vol. 160, no. 13–14, pp. 1501–1506, 2010.

[91] X. Crispin et al., "The Origin of the High Conductivity of Poly(3,4-ethylenedioxythiophene)–Poly(styrenesulfonate) (PEDOT–PSS) Plastic Electrodes," *Chem. Mater*., vol. 18, no. 18, pp. 4354–4360, 2006.

[92] A. M. Nardes, R. A. J. Janssen, and M. Kemerink, "A morphological model for the solvent-enhanced conductivity of PEDOT:PSS thin films," *Adv. Funct. Mater*., vol. 18, no. 6, pp. 865–871, 2008.

[93] J. H. Page, F. Hajighasemi, and S. Tajik, "Assessment of Cytotoxicity of Dimethyl Sulfoxide in Human Hematopoietic Tumor Cell Lines," *Iranian Journal of Blood & Cancer,* vol. 9, no. 2, pp. 48–53, 2017.

[94] J. C. C. Haumeil and P. A. Rnaud, "Evaluation of the Cytotoxicity Effect of Dimethyl Sulfoxide (DMSO) on Caco2 / TC7 Colon Tumor Cell Cultures," *Biol. Pharm. Bull,* vol. 25, no. 12, pp. 1600–1603, 2002.

[95] M. J. O'Connell et al., "Reversible water-solubilization of single-walled carbon nanotubes by polymer wrapping," *Chem. Phys. Lett.*, vol. 342, no. 3–4, pp. 265–271, 2001.

[96] X. Luo, C. L. Weaver, D. D. Zhou, R. Greenberg, and X. T. Cui, "Highly stable carbon nanotube doped poly(3,4-ethylenedioxythiophene) for chronic neural stimulation," *Biomaterials*, vol. 32, no. 24, pp. 5551–5557, 2011.

[97] C. Peng, J. Jin, and G. Z. Chen, "A comparative study on electrochemical co-deposition and capacitance of composite films of conducting polymers and carbon nanotubes," *Electrochim. Acta*, vol. 53, no. 2, pp. 525–537, 2007.

[98] X. Wang et al., "Fabrication of Ultralong and Electrically Uniform Single-Walled Carbon Nanotubes on Clean Substrates," *Nano Lett.*, vol. 9, no. 9, pp. 3137–3141, 2009.

[99] B. Bachmann et al., "All-inkjet-printed gold microelectrode arrays for extracellular recording of action potentials," *Flex. Print. Electron.*, vol. 2, no. 3, p. 035003, 2017.

[100] G. C. Jensen, C. E. Krause, G. A. Sotzing, and J. F. Rusling, "Inkjet-printed gold nanoparticle electrochemical arrays on plastic. Application to immunodetection of a cancer biomarker protein," *Phys. Chem. Chem. Phys.*, vol. 13, no. 11, pp. 4888–4894, 2011.

[101] Z. Xu et al., "Real-time in situ sensing of multiple water quality related parameters using micro-electrode array (MEA) fabricated by inkjet-printing technology (IPT)," *Sensors Actuators, B Chem.*, vol. 237, pp. 1108–1119, 2016.

[102] A. Lesch et al., "Fabrication of soft gold microelectrode arrays as probes for scanning electrochemical microscopy," *J. Electroanal. Chem.*, vol. 666, pp. 52–61, 2012.

[103] Y. Kim, J. W. Kim, J. Kim, and M. Noh, "A novel fabrication method of Parylene-based microelectrodes utilizing inkjet printing," *Sensors Actuators, B Chem.*, vol. 238, pp. 862–870, 2017.

[104] C. Hu, X. Bai, Y. Wang, W. Jin, X. Zhang, and S. Hu, "Inkjet printing of nanoporous gold electrode arrays on cellulose membranes for high-sensitive paper-like electrochemical oxygen sensors using ionic liquid electrolytes," *Anal. Chem.*, vol. 84, no. 8, pp. 3745–3750, 2012.

[105] E. Vitoratos, S. Sakkopoulos, N. Paliatsas, K. Emmanouil, and S. A. Choulis, "Conductivity Degradation Study of PEDOT : PSS Films under Heat Treatment in Helium and Atmospheric Air," *J. Organ. Polym. Mat,.* vol. 2, pp. 7–11, 2012.

[106] C. Yang, C.-Y. Vanessa Li, F. Li, and K.-Y. Chan, "Complex Impedance with Transmission Line Model and Complex Capacitance Analysis of Ion Transport and Accumulation in Hierarchical Core-Shell Porous Carbons," *J. Electrochem. Soc.*, vol. 160, no. 4, pp. 271–278, 2013.

[107] L. Turnbull, E. Dian, and G. Gross, "The string method of burst identification in neuronal spike trains," *J. Neurosci. Methods*, vol. 145, no. 1–2, pp. 23–35, 2005.

[108] A. Mazzoni, F. D. Broccard, E. Garcia-Perez, P. Bonifazi, M. E. Ruaro, and V. Torre, "On the dynamics of the spontaneous activity in neuronal networks," *PLoS One*, vol. 2, no. 5, 2007.

[109] J. V. Selinger, N. V. Kulagina, T. J. O'Shaughnessy, W. Ma, and J. J. Pancrazio, "Methods for characterizing interspike intervals and identifying bursts in neuronal activity," *J. Neurosci. Methods*, vol. 162, no. 1–2, pp. 64–71, 2007.

[110] M. Chiappalone, A. Novellino, I. Vajda, A. Vato, S. Martinoia, and J. van Pelt, "Burst detection algorithms for the analysis of spatio-temporal patterns in cortical networks of neurons," *Neurocomputing*, vol. 65–66, no. SPEC. ISS., pp. 653–662, 2005.

[111] F. E. Kapucu, J. M. A. Tanskanen, J. E. Mikkonen, L. Ylä-Outinen, S. Narkilahti, and J. A. K. Hyttinen, "Burst analysis tool for developing neuronal networks exhibiting highly varying action potential dynamics," *Front. Comput. Neurosci*., vol. 6, no. June, pp. 1–14, 2012.

[112] D. A. Wagenaar, J. Pine, and S. M. Potter, "An extremely rich repertoire of bursting patterns during the development of cortical cultures," *BMC Neurosci*., vol. 7, pp. 1–18, 2006.

[113] V. Pasquale, S. Martinoia, and M. Chiappalone, "A self-adapting approach for the detection of bursts and network bursts in neuronal cultures," *J. Comput. Neurosci*., vol. 29, no. 1–2, pp. 213–229, 2010.

[114] D. Danovi et al., "A High-Content Small Molecule Screen Identifies Sensitivity of Glioblastoma Stem Cells to Inhibition of Polo-Like Kinase 1," *PLoS One,* vol. 8, no. 10, 2013.

[115] H. Carén et al., "Glioblastoma stem cells respond to differentiation cues but fail to undergo commitment and terminal cell-cycle arrest," *Stem Cell Reports*, vol. 5, no. 5, pp. 829–842, 2015.

[116] T. M. Fael Al-Mayhani et al., "An efficient method for derivation and propagation of glioblastoma cell lines that conserves the molecular profile of their original tumours," *J. Neurosci. Methods*, vol. 176, no. 2, pp. 192–199, 2009.

[117] E. M. Kenney-Herbert, S. L. R. Ball, T. M. F. Al-Mayhani, and C. Watts, "Glioblastoma cell lines derived under serum-free conditions can be used as an in vitro model system to evaluate therapeutic response," *Cancer Lett*., vol. 305, no. 1, pp. 50–57, 2011.